A numerical study on the dissipation mechanisms in sloshing flows induced by violent and high frequency accelerations.
Part I: Theoretical formulation and numerical investigation

S. Marrone and A. Colagrossi[*]

CNR-INM, INstitute of Marine Engineering,

Via di Vallerano 139, 00128 Rome, Italy.

F. Gambioli

Airbus Operations Ltd Pegasus House,

Aerospace Avenue, Filton, Bristol,

BS43 7PA, England, U.K.

L. González-Gutiérrez

School of Naval Engineering,

Universidad Politécnica de Madrid,

Avda. de la Memoria 4 28040 Madrid Spain

(Dated: November 15, 2021)

Abstract

The sloshing motion of a confined liquid inside a vertically moving tank is analyzed in the present series of paper. The main objective of the study is to understand the multiple resulting energy dissipation mechanisms, namely wall-liquid impacts and free surface phenomena, among others. This analysis is connected to the damping effects on the aircraft wings caused by the liquid action inside the fuel tanks. Due to the complexity and non-linearity of the flow generated inside the tank, only experiments or efficient numerical solvers are suitable for studying the problem. In this paper, the tank-fluid system is periodically excited with a prescribed law of motion and the non-linear features are observed, the force between the wall and the fluid and the global energy balance are computed. A weakly-compressible smoothed particle hydrodynamics model (WCSPH), has been reformulated and adapted to this kind of violent and turbulent flow. The evolution of the different terms that appear in the energy conservation law are computed, and the formulation is compared to other alternatives where the advantages of the present formulation are indicated. The comparison with the experimental results and the fluid-structure interaction case is carried out in Paper II [Marrone,Colagrossi,...Gonzalez,"A numerical study on the dissipation mechanisms in sloshing flows induced by violent and high frequency accelerations. Part II: comparison against experimental data."] of this work.

---

* andrea.colagrossi@cnr.it

I. INTRODUCTION

There are an important number of situations involving a liquid that evolves dynamically in a confined portion of space. These situations can be found either when the liquid, typically a kind of fuel, is transported from different (air)ports or when it is used as Tuned Liquid Damper (TLD) to counteract the motions caused by an external agent, such as building motion during earthquakes, ship rolling motion due to waves or any other complex dynamic phenomena. Focusing on the aim of improving the safety and efficiency of fuel transport, this is an open problem for the engineering community, which has evolved to match the fast-paced nature of the human race. Starting from the shape and size evolution of the trucks that transport fuel, and taking into account the design of the tanks and containers used for fuel transport by ship or train, the behaviour of the fluid inside liquid containers and fuel tanks has been widely studied for many decades over this and the last century. All the situations that have been described imply that the confined liquid moves inside the tank with high accelerations and strong wall impacts, and are commonly identified as examples of "sloshing flows". Lately, a typical and attractive example of this kind of confined flow that has received attention is found in the kerosene containers placed below aircraft wings, where the fluid is moved by violent structural loads coming in turn from external wind gusts and air turbulence. In this application, the fluid is vertically accelerated up to typical values in the order of $10g$, which results in amplitudes comparable to the tank dimensions and frequencies higher than 5 Hz. In this context several experiments, such as [37], have demonstrated that fluid motion plays a role on the wing structure, acting as a damper. In these conditions the initial stages of the flow evolution are driven by intense breaking of the free surface due to the impulsive heaving motion of the tank, also inducing a detachment of the fluid from the tank walls. The previous flow regime is somehow different to what is normally described as a "sloshing flow", as the fluid is continuously broken into more and more jets and drops whilst violently slamming alternately upward and downward against the top and bottom walls. It is therefore necessary to clarify that under the name of "sloshing flows" a very wide variety of fluid dynamics behaviours are included. Seminal books, such as the ones by [23] or [1] present a thorough review of sloshing dynamics and its applications. Normally, in the common literature the term "sloshing flow" is used to describe those situations when the tank acceleration decreases to values smaller than 2-3g, and the flow is essentially driven by gravity forces. Due to this terminology, and for the sake of clarity, in the present paper the initial stages of such violent flow, when it is essentially driven by inertial forces

due to vertical accelerations considerably larger than the gravitational ones, will be referred to as "shaken flow". These very violent flows have been rarely addressed in the literature and only very recently they have received attention [9, 15, 18, 37, 43] fostered by the European H2020 project SLOWD [24].

Violent sloshing flows can be studied computationally using different numerical techniques. There exist relevant studies based on the Finite Volume techniques, such as the ones proposed by [10, 25, 26], that are examples of the different strategies used to tackle different sloshing problems. In this work, the lagrangian meshless method Smoothed Particle Hydrodynamics (SPH) has been used instead to discretize the liquid phase of the problem, while the gas phase has not been explicitly included in the simulation, the assumption being that it plays a negligible role. The SPH method was conceived in 1977 by [27, 34] to solve astrophysics problems, but due to its flexibility it quickly spread over into different disciplines, including free surface flows [40]. Several complex problems in computational engineering have been accurately solved by SPH (see, *e.g.*,[19, 28, 46], which includes fluid-structure interaction problems [48] and violent sloshing problems in the presence of complex geometries [50]. Recently, a thorough validation on sloshing flows occurring in tanks of different shapes has been carried out by Green[29]. As a consequence, SPH can be presented as an efficient methodology when compared to mesh-based methods to simulate free surface flows, and precisely those including violent sloshing. More in depth, this paper is not limited to obtaining accurate simulations of the violent vertical sloshing flows described above; it also attempts the study of the energy dissipation mechanisms that occur in these kinds of violent and confined flows which, eventually, are of interest in aeronautics applications. There is a vast literature related to energy dissipation in sloshing flows, especially in TLD studies for seismic applications (see, *e.g.* [16, 42]). Energy dissipation in lateral sloshing was treated from a theoretical point of view in [20] and by several numerical and semi-analytical works [45, 49]. However, in all those works the study was limited to either roll or sway sloshing which are rather different from the violent vertical sloshing flows addressed in the present research.

To achieve this goal using the SPH methodology, important particular aspects of the classical SPH method should be revisited. First, the pressure fields obtained during the violent impacts should be accurately computed, which implies the presence of diffusive terms in the mass conservation equation as the ones proposed by [3] with the δ-SPH formulation. Second, the possibility of computing negative pressure fields that produce undesired effects denominated in the SPH literature as "tensile instability" must be avoided. In order to limit the "tensile instability"

4

onset, a particle shifting technique, as the one reported by [50] can be adopted. The latter allows, at the same time, the achievement of making accurate computations with little spurious energy dissipation by enforcing uniform particle distributions. Third, assuming that the flow is highly turbulent and that multiple scales are involved in the fluid diffusion process, only the largest scales are included in the simulation due to the limited computational capacity. The sub-grid scales must be included using a Large Eddy Simulation (LES) model such as the one described in [21]. Finally, the SPH scheme formulated for these kinds of flows should be robust enough to deal with highly complex and fragmented free surfaces. Most of the improvements required for our particular SPH formulation have been previously presented in the works by [3, 5, 21, 51] and applied to less confined and violent flows. In the present work those schemes are merely restated, and the reader is encouraged to find more details on the numerical implementation in the referred works.

This work is separated in two parts (Parts I and II), and the first one deals with the theoretical basis of the formulation and fundamentals of the energy dissipation mechanisms, where this methodology is applied to a sloshing tank with prescribed vertical periodic motion. In the second part (Part II), the method is applied to a wider range of cases, which include external damped oscillations, the coupled fluid-structure interaction (FSI) version of the problem with a spring-damper system and finally an experimental comparison of the previous results. This first part I is organized as follows: Sec. III briefly explains the mathematical model used, including the main assumptions that are made. Then, energy terms arising from energy balance are analyzed in Sec. IV. Main aspects of the LES turbulent model are summarized in Sec. V. Then, in Sec. VI emphasis is given to the dissipation terms introduced by the discrete SPH formulation. Finally, Sec. VII is dedicated to presenting a set of numerical test cases where the main findings are discussed. As mentioned before, Part II of the paper will complement the perspective given in this first part, where the experimental validation will also be included.

II. PROBLEM DESCRIPTION

In [37] a violent sloshing flow in a vertically moving tank with a single degree of freedom has been experimentally studied. In the present work the conditions adopted in that experimental campaign are considered for the numerical simulations. In [37] a tank with geometry 10x6x6 cm is connected to a set of 6 springs, 3 on the upper side and 3 on the lower side. The tank is filled up to 50 % of its volume with a water mass of $m_l = 0.18$ kg and, when the springs are released,

oscillates at a characteristic frequency of f_0 = 6.5 Hz. More details about the experiment are also given in the second part of this paper (Part II).

The problem geometry considered in the present work is two-dimensional and is sketched in Fig. 1, where L = 0.1 m, D = 0.06 m and H = 0.03 m. In the same plot the liquid menisci due to the contact angle θ between the lateral walls and the liquid surface are depicted and enlarged in the inset. They play a relevant role during the initial stages of the flow evolution as further discussed in the following pages.

The Reynolds number of the problem is defined as Re = $U_{max}L/\nu$ where U_{max} is the maximum tank velocity and ν the kinematic viscosity of the fluid. In the present work only water is considered, while in the second part of the paper (Part II) oil sloshing is also analysed. For the simulation analysed here the same order of magnitude of the initial acceleration obtained in [37] is retained, resulting in a flow Reynolds number of order $O(10^5)$. In these conditions the flow starts developing a Rayleigh-Taylor instability consequent to the first vertical acceleration, followed by a first roof impact. As a result of the rapid tank motions, a highly turbulent flow slamming alternately against the bottom and the roof of the tank occurs. Note that in the right plot of Fig. 1 the case where the tank is subjected to both rotation and translations is represented, and the governing equations below will address this general framework. However, the numerical simulations will address only problems where the tank motion is limited to the vertical translation (see Sec. IV A). Differently from the experimental case, in which the motion slowly decays and which will be addressed in the second part of this paper (Part II), here we consider the tank when subjected to a periodic forced heaving motion.

III. GOVERNING EQUATIONS

In the present work a two-dimensional fluid domain Ω delimited by a free surface $\partial\Omega_F$ and closed solid surface $\partial\Omega_B$ is considered (see left plot of Fig. 1). The domain Ω contains only a liquid phase and $\partial\Omega_B$ represents the internal surface of a moving tank. The governing equations adopted are the Navier-Stokes equations (NSE) for a single-phase weakly-compressible fluid:

$$\begin{cases} \dfrac{D\rho}{Dt} = -\rho\operatorname{div}(\boldsymbol{u})\,, & \dfrac{D\boldsymbol{u}}{Dt} = \boldsymbol{g} + \dfrac{\operatorname{div}(\mathbb{T})}{\rho} \\[2mm] \dfrac{De}{Dt} = \dfrac{\mathbb{T}:\mathbb{D}}{\rho}\,, & \dfrac{D\boldsymbol{r}}{Dt} = \boldsymbol{u}\,, \qquad p = f(\rho)\,, \end{cases} \tag{1}$$
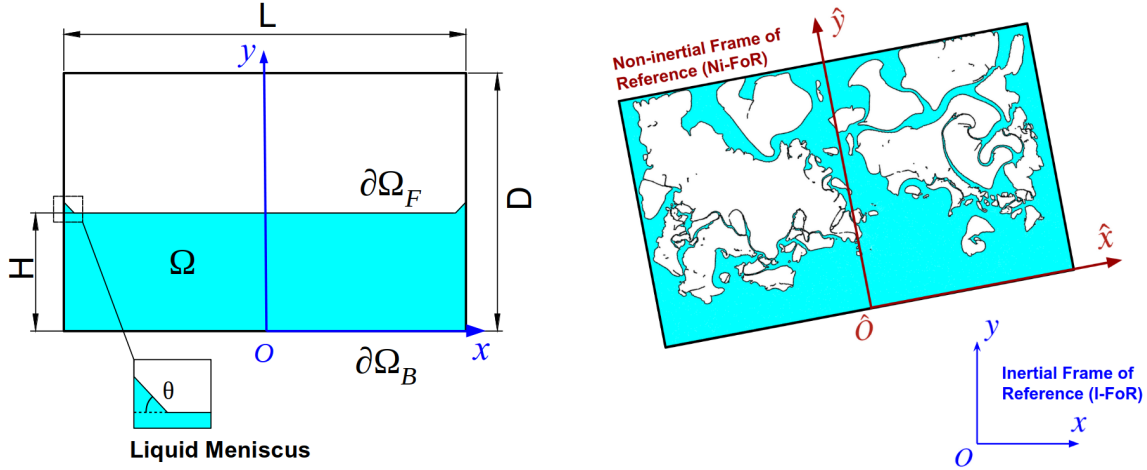
6

FIG. 1: Left plot: sketch of the problem geometry. Right plot: example of the tank motion and consequent flow evolution.

where D/Dt represents the Lagrangian derivative, $\boldsymbol{u}$ the flow velocity, $\boldsymbol{r}$ the position of the material points, ρ the fluid density, e the specific internal energy, $\mathbb{T}$ the stress tensor, $\mathbb{D}$ the rate of strain tensor and $\boldsymbol{g}$ is a generic specific body force. Thermal conductivity and surface tension effects are neglected, and the liquid is considered to be Newtonian *i.e*: $\mathbb{T} = [-p + \lambda \operatorname{div}(\boldsymbol{u})] \, \mathbb{I} + 2 \mu \, \mathbb{D}$, where μ and λ are the primary and secondary dynamic viscosity of the liquid and $\mathbb{I}$ the identity tensor.

The Eq. (1) can be either solved in an Inertial Frame of Reference (I-FoR) where the tank is moving, or in a Non-inertial Frame of Reference (Ni-FoR) moving with tank motion (see right plot of Fig. 1). In the former case the force field $\boldsymbol{g}$ would be the gravitational acceleration while in the second case the non-inertial accelerations $\boldsymbol{f}_{NI}$ due to the tank motion need to be added:

$$
\begin{cases}
\dfrac{D\rho}{Dt} = -\rho \operatorname{div}(\hat{\boldsymbol{u}}), & \dfrac{D\hat{\boldsymbol{u}}}{Dt} = \hat{\boldsymbol{g}} + \boldsymbol{f}_{NI} + \dfrac{\operatorname{div}(\hat{\mathbb{T}})}{\rho} \\[4mm]
\dfrac{De}{Dt} = \dfrac{\hat{\mathbb{T}} : \hat{\mathbb{D}}}{\rho}, & \dfrac{D\hat{\boldsymbol{r}}}{Dt} = \hat{\boldsymbol{u}}, \qquad p = f(\rho),
\end{cases}
\tag{2}
$$

where the symbol ^ is used to identify the quantities in the Ni-FoR. There are quantities like ρ, p, $\operatorname{div}(\boldsymbol{u})$, $\|\mathbb{D}\|$ and ($\mathbb{T} : \mathbb{D}$) which are invariant for the change of the frame of reference, others like the positions, velocities and accelerations, which are dependent on the tank motion, and still others whose dependency is linked only to the tank rotations, like the tensors $\mathbb{D}$, $\mathbb{T}$ and the vector $\boldsymbol{g}$.

While the use of I-FoR or Ni-FoR does not affect the evaluation of the energy dissipated by the liquid motions, the numerical procedures can be affected by this choice. Due to its easier

implementation the Ni-FoR is generally preferred, and also because it avoids numerical errors related to the tank motion. This is, indeed, the choice made in the present work.

Besides the technical numerical aspects, the energy balance written in both the frames of reference can be useful for the data analysis and the comparison against the experimental measurements, see the second part of this paper (Part II). This aspect will be addressed next.

For the liquid medium, we consider the effects of entropy/temperature on pressure to be negligible. Therefore, the pressure p is considered to depend only on the density. Furthermore, since a weakly-compressible regime is assumed, a simple linear equation of state can be adopted:

$$p = c_0^2 (\rho - \rho_0), \tag{3}$$

where c_0 is the speed of sound (assumed constant) of the liquid medium and ρ_0 the density at the free-surface (where p is assumed to be equal to zero).

The weakly-compressible regime implies the following requirement:

$$c_0 \geq \max \left(10 U_{max}, 10 \sqrt{\frac{(\Delta p)_{max}}{\rho}} \right) \tag{4}$$

where U_{max} and $(\Delta p)_{max}$ respectively are the maximum fluid speed and the maximum pressure variation expected (with respect to the zero pressure free-surface level) in Ω (see [36]). For numerical purposes, in order to avoid too small time steps, in the simulations c_0 is chosen smaller than its physical counterpart. Constraint (4) however, has to be respected to guarantee the weakly-compressible regime and this condition has to be verified throughout the simulations.

To summarize, the main simplifications adopted in the model are:

- a two-dimensional framework;

- the air phase is neglected (only the liquid phase is modelled);

- thermal conductivity and surface tension effects are neglected;

- weakly-compressible regime is always attained using an artificial speed of sound.

Although the first two may be regarded as strong approximations for modelling violent sloshing flows, we will show that it is possible to obtain a fair estimation of the dissipated energy when comparing the numerical outputs against experimental measurements. It is worth noting that in [33] it is shown that when modelling breaking waves the differences between 2D and 3D

frameworks are generally small, the difference of the dissipated energy being smaller than 10% even after a few wave periods from the first breaking event. Analogous results have been obtained in [7, 8] for the study of the mechanical energy dissipation induced by sloshing and wave breaking in a fully coupled angular motion system. In principle, the inverse cascade which characterises 2D turbulent flows could represent a substantial hindrance to the simulation of the considered turbulent 3D flow. However, the considered violent free-surface flow conditions are essentially different from those encountered in homogeneous turbulence and the time interval between two impacts is too short to allow the inverse cascade to take place. This is also linked to the highly deformed free surface which strongly interacts with the vortical structures, further limiting the possibility of vortex merging.

Regarding the use of a single-phase model and neglecting the role of the air contained in Ω, in [36] it was shown that the evaluation of the energy dissipation in violent flows even within this hypothesis can be still accurate enough. On the other hand, this does not mean that the role of the air phase cannot play a relevant role on fluid dynamics, especially in terms of local pressure and velocity fields.

As far as the surface tension is concerned, this is relevant above all during the initial stage. Indeed, in the next sections it will be shown that during the initial intense vertical acceleration, a Rayleigh–Taylor instability develops. The latter is triggered by the fluid meniscus formed at the intersection between the lateral walls and the liquid surface. However, after that stage, for the velocity and length scales considered in this work the surface tension effect on the energy dissipation is negligible as shown in [9]. Therefore, in the numerical simulations we neglect the surface tension terms but in the initial fluid setup we assign the free-surface deformation due to the meniscus at the wall with an angle $\theta = 45°$ (see left plot of Fig. 1). Finally, concerning the use of artificial speed of sound, as discussed in [35] and in [38], if the weakly-compressible regime is attained the energy dissipation linked to the water impacts using Eqs. (1) remains very close to the one predicted by incompressible flow models.

A. Boundary conditions

The governing Eq. (1) needs the enforcement of kinematic and dynamic free-surface boundary conditions on $\partial\Omega_F$, while on the solid surfaces $\partial\Omega_B$ the adherence boundary condition (no-slip) needs to be enforced. Concerning the former, free-surface boundary conditions are intrinsically

satisfied in SPH methods (see [14]). On the other hand, in SPH it is difficult to resolve thin wall boundary layer (WBL) conversely to mesh-based methods. Indeed, the stretching of the computational points close to the walls implies large CPU costs linked to the explicit time integration of the scheme, as the time steps decrease proportionally to the particle size. Consequently, if the low viscosity of the fluid implies a very thin WBL, which cannot be numerically resolved, a simple no-penetration boundary condition (free-slip) is preferred.

It is generally difficult to know a priori the role played by the viscous WBL, since it can depend on the problem at hand. Regarding the flows investigated in this article, the Reynolds number is close to 500,000 and an order of magnitude of the WBL thickness can be estimated through the Blasius equation. As discussed in Sec. VII it will turn out that for the spatial resolution adopted it is not possible to resolve the WBL regions, and for this reason the free-slip conditions are enforced. Conversely, in the second part of this paper (Part II), simulations with oil are also performed, and for these the Reynolds number decreases down to 4,660. In such a condition, with the spatial resolutions adopted, it is possible to resolve the WBL regions, and therefore, for these simulations the no-slip conditions are enforced.

For the simulations with water, in order to estimate the relevance of the free-slip condition adopted, simulations with no-slip conditions are also performed. In the latter case, the boundary layer will be inevitably overestimated. The comparison of the results will however provide a clue on the appropriateness of the free-slip approximation. Indeed, if the energy dissipation evaluated with both the boundary conditions remains close, we can establish that the role of WBL are negligible in those kinds of flows.

B. Sub-grid models

Because of the high Reynolds number related to the simulations with water, in the numerical scheme a sub-grid model for the turbulent viscosity is needed. For this purpose the works by [22], [5] are considered, where an LES modeling is rewritten in a quasi-Lagrangian formalism and introduced in the SPH system of equations.

Even if we are limiting our analysis to a two-dimensional framework, in order to perform long-time simulations the number of particles has to be kept reasonably low due to CPU costs. On the other hand, in order to have a meaningful LES description of the flow, the spatial resolution needs to be sufficiently high to capture the main vortical structures. These two limits are discussed in

10

depth in Section VII.

In [12, 13] a simple Smagorinsky model is adopted for simulating breaking waves. The same choice has been made in the present work. A more complex LES model can be considered for future work such as the one used in [32], which in any case needs to be studied and adapted in the SPH framework. Furthermore, advanced LES models are especially needed to accurately model the turbulent flows in proximity to a solid surface. In our problem the relevant turbulent flow is in the bulk of the flow, and the role of the solid boundary is not so relevant. It is worth noting that turbulence models in violent free-surface and multiphase flows still remain an open problem (see *e.g.* [31]).

C. Energy dissipation in liquid impacts

As discussed in [35], during liquid impacts energy losses occur. The actual weakly-compressible nature of the liquids implies that, during impacts, a portion of the mechanical energy is converted into internal compressible energy in the form of acoustic waves, and then dissipated through primary and secondary viscous terms. When adopting the incompressible flow assumption this behaviour is different since the same amount of energy is instantaneously lost when the liquid impact occurs [52]. In the present scheme, in which an artificial speed of sound is adopted, the real physical dissipation mechanism is mimicked, and it acts mainly through numerical diffusive terms (as discussed in [38, 39], see also Sec. VI). Incidentally, note that in [35, 36] it has been shown that the amount of energy dissipated through liquid impacts in the weakly-compressible SPH model is equal to the one dissipated in incompressible flow solvers.

IV. ENERGY CONSERVATION

Considering the I-FoR, the power that the fluid transfers (or receives if negative in value) to the solid boundary $\partial\Omega_B$ is given by integrating the elementary power acting on each surface element of $\partial\Omega_B$, due to the stress forces:

$$\mathcal{P}_{fluid/body} = -\int_{\partial\Omega_B} \mathbb{T}\boldsymbol{n_B} \cdot \boldsymbol{u_B}\, dS \tag{5}$$

$\boldsymbol{u_B}$ being the velocity of the tank and $\boldsymbol{n_B}$ the normal unit vector pointing inward toward the solid body. The power $-\mathcal{P}_{fluid/body} = \mathcal{P}_{body/fluid} := \mathcal{P}_{ext}$ has to be converted into the total energy of

11

the fluid. Considering the Newtonian nature of the fluid, the external power can be split into components:

$$\mathcal{P}_{ext} = -\int_{\partial\Omega_B} p\, \boldsymbol{n_B} \cdot \boldsymbol{u_B}\, dS \;+\; \mu \int_{\partial\Omega_B} (\boldsymbol{\omega} \times \boldsymbol{n_B}) \cdot \boldsymbol{u_B}\, dS \;+\; \lambda \int_{\partial\Omega_B} \text{div}(\boldsymbol{u})\, \boldsymbol{n_B} \cdot \boldsymbol{u_B}\, dS \qquad (6)$$

linked to the action of pressure forces, the friction on the wall and to the viscous-compressibility. The last one is generally negligible in the weakly-compressible regime, even when impact events occur.

The surface integral (5) can be extended to the whole boundary $\partial\Omega$ since no power can act on the fluid through the free surface. An equivalent way to define the power using the divergence theorem gives therefore:

$$\mathcal{P}_{ext} = \int_\Omega \text{div}\,(\mathbb{T}\boldsymbol{u}) dV \qquad (7)$$

The right hand side of Eq. (7) can be expressed as :

$$\mathcal{P}_{ext} = \int_\Omega (\text{div}\,\mathbb{T}) \cdot \boldsymbol{u}\, dV + \int_\Omega \mathbb{T} : \mathbb{D}\, dV \qquad (8)$$

being the operation $\mathbf{X} : \mathbf{Y}$ the inner product between the generic tensors $\mathbf{X}$ and $\mathbf{Y}$. The external power, $\mathcal{P}_{ext}$ is therefore separated in two different parts.

Using momentum conservation (the second equation in (1) and assuming that the body force $\boldsymbol{g}$ admits a potential, the first term of the right hand side of (8) can be expressed as:

$$\int_\Omega \text{div}\,(\mathbb{T}) \cdot \boldsymbol{u}\, dV = \dot{\mathcal{E}}_K + \dot{\mathcal{E}}_P \qquad (9)$$

$\mathcal{E}_K$ and $\mathcal{E}_P$ being the kinetic and the potential energies respectively, while $\dot{X}$ indicates time derivative of a generic quantity X. Their sum gives the mechanical energy of the fluid, *i.e.* $\mathcal{E}_M := \mathcal{E}_K + \mathcal{E}_P$.

The second term of the right hand side of (8) is the internal energy time derivative $\dot{\mathcal{E}}_I$ (see Eq. (1)). It can be expressed as:

$$\dot{\mathcal{E}}_I = \frac{d}{dt} \int_\Omega e\rho\, dV = \int_\Omega \mathbb{T} : \mathbb{D}\, dV = \dot{\mathcal{E}}_C - \mathcal{P}_V \qquad (10)$$

where the two terms on the right hand side are:

$$\mathcal{P}_V := -2\mu \int_\Omega \mathbb{D} : \mathbb{D}\, dV - \lambda \int_\Omega (\text{div}\boldsymbol{u})^2\, dV\,, \qquad \dot{\mathcal{E}}_C := -\int_\Omega p\, \text{div}(\boldsymbol{u})\, dV \qquad (11)$$

The term $\mathcal{P}_V$ is the classical viscous dissipation term for a Newtonian fluid which is always a non-positive function in accordance with the second law of thermodynamics. Regarding the term $\dot{\mathcal{E}}_C$,

this is associated with the fluid compressibility and is a purely reversible term. Using the equation of state and the continuity equation, the elastic potential energy $\mathcal{E}_C$ can be evaluated by integration. In the case where a simple linear state equation is used, this term becomes:

$$\mathcal{E}_C = \mathcal{E}_C(\rho_0) + c_0^2 \int_\Omega \left[\log\left(\frac{\rho}{\rho_0}\right) + \frac{\rho_0}{\rho} - 1 \right] \rho \, dV \tag{12}$$

where $\mathcal{E}_C(\rho_0)$ is the internal energy value set for the fluid at rest condition (*i.e.* $\rho = \rho_0$). Following the work of [35], during fluid impacts acoustic waves are generated, and during the post-impact stage energy is transferred back and forth from mechanical energy $\mathcal{E}_M$ to $\mathcal{E}_C$ and vice versa. The acoustic waves are rapidly dissipated.

In summary, the energy balance within the I-FoR (8) is expressed as:

$$-\mathcal{P}_{ext} + \dot{\mathcal{E}}_M + \dot{\mathcal{E}}_C = \mathcal{P}_V \leq 0 \tag{13}$$

Conversely, if a Ni-FoR is considered the above balance becomes:

$$-\mathcal{P}_{NF} + \dot{\hat{\mathcal{E}}}_M + \dot{\mathcal{E}}_C = \mathcal{P}_V \leq 0 \tag{14}$$

where $\dot{\hat{\mathcal{E}}}_M$ is the time variation of the mechanical energy evaluated in the Ni-FoR whereas $\mathcal{P}_{NF}$ is the power linked to the non-inertial forces:

$$\mathcal{P}_{NF} = \int_\Omega \rho \, \boldsymbol{f}_{NI} \cdot \hat{\boldsymbol{u}} \, dV \tag{15}$$

It is worth noting that the term $\dot{\mathcal{E}}_C$ and $\mathcal{P}_V$ are both invariant with respect to the frame of reference adopted. From the latter consideration and combining the two Eqs. (13), (14), it follows that:

$$\dot{\mathcal{E}}_M = \dot{\hat{\mathcal{E}}}_M + (\mathcal{P}_{ext} - \mathcal{P}_{NF}) \tag{16}$$

For the flow studied in this work the mechanical energy of the tank in the I-FoR is generally much greater than the corresponding energy in the Ni-FoR, *i.e.* $\mathcal{E}_M \gg \hat{\mathcal{E}}_M$. Indeed the former also contains the mechanical energy due to the tank motion, as further discussed in the next subsection.

A. Energy balance for a translating tank

In this subsection we consider the fact that in our problem the velocity of the tank is just a vertical translation $\boldsymbol{u_B} = v_{Tank}\,\boldsymbol{j}$. Within this hypothesis the external power (5) can be rewritten as:

$$\mathcal{P}_{ext} = v_{Tank}\,\boldsymbol{j} \cdot \int_{\partial\Omega_B} \mathbb{T}\boldsymbol{n}_B \, dS = v_{tank}\,\boldsymbol{j} \cdot \boldsymbol{F}_{tank/fluid} \tag{17}$$

13

Considering Eq. (6) (neglecting the last term) and that the flow is planar (*i.e.* $\boldsymbol{\omega} = \omega\,\boldsymbol{k}$) the above equation is reformulated as:

$$
\begin{cases}
\mathcal{P}_{ext} = v_{tank}\,\boldsymbol{j} \cdot (\boldsymbol{F}^{press}_{tank/fluid} + \boldsymbol{F}^{visc}_{tank/fluid}) \\[2mm]
\boldsymbol{F}^{press}_{tank/fluid} := \displaystyle\int_{\partial\Omega_B} -p\,\boldsymbol{n}_B\,dS\,, \quad \boldsymbol{F}^{visc}_{tank/fluid} := \mu \int_{\partial\Omega_B} \omega\,\boldsymbol{\tau}_B\,dS
\end{cases}
\tag{18}
$$

where $\boldsymbol{F}^{press}_{tank/fluid}$ and $\boldsymbol{F}^{visc}_{tank/fluid}$ are the forces exerted by the tank walls on the fluid due to the pressure and friction actions and $\boldsymbol{\tau}_B := (\boldsymbol{k} \times \boldsymbol{n}_B)$ is the tangential unit vector at the tank surface.

In the present work the tank has a simple rectangular shape, and hence, the two force components along the vertical direction are expressed as:

$$
\begin{cases}
\boldsymbol{j} \cdot \boldsymbol{F}^{press}_{tank/fluid} = \left(\displaystyle\int_{Bottom} p\,dS - \int_{Roof} p\,dS \right) \\[3mm]
\boldsymbol{j} \cdot \boldsymbol{F}^{visc}_{tank/fluid} = \mu \left(\displaystyle\int_{Rwall} \omega\,dS - \int_{Lwall} \omega\,dS \right)
\end{cases}
\tag{19}
$$

where *Rwall* and *Lwall* are the right and the left sides of the vertical tank respectively. Because of the high Reynolds number treated in this work, the viscous component of the force is always negligible with respect to the pressure component. Therefore, the external power can be expressed as:

$$
\mathcal{P}_{ext} = v_{tank} \left(\int_{Bottom} p\,dS - \int_{Roof} p\,dS \right)
\tag{20}
$$

the above approximation is even more valid if a free-slip boundary condition is enforced along the tank wall.

Beside the splitting into pressure and friction components, force $\boldsymbol{F}_{tank/fluid}$ can be also splitted in a second way:

$$
\boldsymbol{F}_{tank/fluid} = \boldsymbol{F}^{stat}_{tank/fluid} + \boldsymbol{F}^{dyn}_{tank/fluid}\,, \qquad \boldsymbol{F}^{stat}_{tank/fluid} := M_{liquid}\,(g + a_{tank})\,\boldsymbol{j}
\tag{21}
$$

where part of the force is given by the liquid weight $M_{liquid}\,g$ and the inertia due to the tank acceleration a_{tank}, while the remaining part, $\boldsymbol{F}^{dyn}_{tank/fluid}$, is the force that the tank is transferring into the liquid because of its deformation inside the tank.

Integrating the momentum equation in system (2) on the domain Ω, and considering that the non-inertial forces for the case of a pure tank translation are simply given by $\boldsymbol{f}_{NI} = -a_{tank}\,\boldsymbol{j}$, it results that:

$$
\int_{\Omega} \hat{\boldsymbol{a}}\,\rho\,dV = -\int_{\Omega} (g + a_{tank})\,\boldsymbol{j}\,\rho\,dV + \int_{\Omega} \mathrm{div}(\mathbb{T})\,dV = -M\,(g + a_{tank})\,\boldsymbol{j} + \int_{\partial\Omega} \mathbb{T}\,\boldsymbol{n}\,dS
\tag{22}
$$

where $\hat{\boldsymbol{a}}$ is the acceleration of the generic material point in the Ni-FoR. Since the integral is zero on the free surface $\partial\Omega_F$ the last term of (22) is the force $\boldsymbol{F}_{tank/fluid}$. Considering Eq. (21) the above equation becomes:

$$M_{liquid}\,\hat{\boldsymbol{a}}_G \; = \; \boldsymbol{F}_{tank/fluid}^{dyn} \tag{23}$$

where $\hat{\boldsymbol{a}}_G$ is the acceleration of the fluid barycentre in the Ni-FoR. This equation clearly links the force component $\boldsymbol{F}_{tank/fluid}^{dyn}$ with the shaking/sloshing motion of the liquid.

Considering the subdivision of the forces (21) the external power can be also expressed as:

$$\mathcal{P}_{ext} \; = \; v_{tank}\,\boldsymbol{j}\,\cdot\,\boldsymbol{F}_{tank/fluid} \; = \; M_{liquid}\,v_{tank}\,(g\,+\,a_{tank}) \; + \; v_{tank}\,\boldsymbol{j}\,\cdot\,\boldsymbol{F}_{tank/fluid}^{dyn} \tag{24}$$

If we define the "static" mechanical energy of the fluid as:

$$\mathcal{E}_M^{stat} \; := \; \frac{1}{2}\,M_{liquid}\,v_{tank}^2 \; + \; M_{liquid}\,g\,y_{tank}\,, \tag{25}$$

where y_{tank} is the vertical position of the tank bottom with respect to its initial position, it follows that:

$$\mathcal{P}_{ext} \; = \; \dot{\mathcal{E}}_M^{stat} \, + \, \mathcal{P}_{ext}^{dyn}\,, \qquad \mathcal{P}_{ext}^{dyn} \; := \; v_{tank}\,\boldsymbol{j}\,\cdot\,\boldsymbol{F}_{tank/fluid}^{dyn} \tag{26}$$

Combining the energy balance (13) with Eq. (26) we finally get:

$$-\mathcal{P}_{ext}^{dyn} \, + \, \dot{\mathcal{E}}_M^{dyn} \, + \, \dot{\mathcal{E}}_C \; = \; \mathcal{P}_V \, \leq 0 \qquad \mathcal{E}_M^{dyn} \; := \; (\mathcal{E}_M \, - \, \mathcal{E}_M^{stat}) \tag{27}$$

This is how energy balance links the external shaking/sloshing power $\mathcal{P}_{ext}^{dyn}$ with the fluid dissipation $\mathcal{P}_V$. Integrating the above equation in time the energy dissipated by the fluid, $\mathcal{E}_{diss}$, is given by:

$$\begin{cases} \mathcal{E}_{diss} \; = \; \displaystyle\int_{t_0}^t \mathcal{P}_V \, dt \; = \; -\mathcal{W}_{ext}^{dyn} \, + \, \left[\mathcal{E}_M^{dyn} \, - \, \mathcal{E}_M^{dyn}(t_0)\right] + \, [\mathcal{E}_C \, - \, \mathcal{E}_C(t_0)]\,, \\[4mm] \mathcal{W}_{ext}^{dyn} \; := \; \displaystyle\int_{t_0}^t v_{tank}\,\boldsymbol{j}\,\cdot\,\boldsymbol{F}_{tank/fluid}^{dyn}\, dt \end{cases} \tag{28}$$

where t_0 is the initial time for the solution of the governing equations. The term $[\mathcal{E}_C \, - \, \mathcal{E}_C(t_0)]$ is generally negligible within the weakly-compressible assumption and can be disregarded in the evaluation of the dissipated energy.

While the external work performed by the force $\mathcal{W}_{ext}^{dyn}$ can be experimentally evaluated through accelerometers and load cells, this is not the case for the $\mathcal{E}_M^{dyn}$ term. However, as we further discussed in the second part of this work (Part II), when considering violent and decaying sloshing

flows the work $\mathcal{W}_{ext}^{dyn}$ is dominant with respect to the $\mathcal{E}_M^{dyn}$ term, and can provide a good estimation of $\mathcal{E}_{diss}$.

It is worth noting that the $\mathcal{E}_M^{dyn}$ term is not the mechanical energy in the Ni-FoR, $\hat{\mathcal{E}}_M$. Indeed, the mechanical energy in the two different frames of reference can be expressed as:

$$
\begin{aligned}
\mathcal{E}_M &= \frac{1}{2} \int_{\Omega} (\hat{\boldsymbol{u}} + v_{tank}\,\boldsymbol{j}) \cdot (\hat{\boldsymbol{u}} + v_{tank}\,\boldsymbol{j})\, \rho\, dV + \int_{\Omega} g\,(\hat{y} + y_{tank})\, \rho\, dV = \\
&= \hat{\mathcal{E}}_M + \mathcal{E}_M^{stat} + M_{liquid}\, v_{tank}\, \boldsymbol{j} \cdot \hat{\boldsymbol{u}}_G
\end{aligned}
\tag{29}
$$

where $\hat{y}$ is the vertical position of the generic material point in the Ni-FoR and $\hat{\boldsymbol{u}}_G$ is the velocity of the fluid barycentre in the Ni-FoR.

Deriving (29) in time the result is:

$$
\dot{\mathcal{E}}_M^{dyn} = \dot{\hat{\mathcal{E}}}_M + M_{liquid}\, v_{tank}\, \boldsymbol{j} \cdot \hat{\boldsymbol{a}}_G + M_{liquid}\, a_{tank}\, \boldsymbol{j} \cdot \hat{\boldsymbol{u}}_G
\tag{30}
$$

For the case of a pure tank translation the power related to the non-inertial forces (15) is given by:

$$
\mathcal{P}_{NF} = \int_{\Omega} \rho\, \boldsymbol{f}_{NI} \cdot \hat{\boldsymbol{u}}\, dV = -M_{liquid}\, a_{tank}\, \boldsymbol{j} \cdot \hat{\boldsymbol{u}}_G
\tag{31}
$$

Combining Eqs. (23) and (31) with Eq. (30) results in:

$$
\dot{\mathcal{E}}_M^{dyn} = \dot{\hat{\mathcal{E}}}_M + \left(\mathcal{P}_{ext}^{dyn} - \mathcal{P}_{NF} \right).
\tag{32}
$$

which establishes the difference between $\mathcal{E}_M^{dyn}$ and $\hat{\mathcal{E}}_M$. The energy balance of (32) is analogous to the energy balance (16) when the inertial terms due to the tank motion are removed.

The relations derived in the present section will be further inspected through the comparisons between numerical solutions and experimental data in the second part of the paper (Part II).

V. BRIEF RESTATING OF δ-LES-SPH MODEL

In this section the δ-LES-SPH model presented in [5, 39] is briefly recalled. For the sake of brevity only the most relevant information is reported, the interested reader is encouraged to find all the details in the cited articles. The governing Eq. (1) are discretized within the Smoothed

Particle Hydrodynamics context as follows:

$$
\begin{cases}
\dfrac{d\rho_i}{dt} = -\rho_i \sum_j (\boldsymbol{u}_{ji} + \delta\boldsymbol{u}_{ji}) \cdot \nabla_i W_{ij}\, V_j \; + \; \sum_j (\rho_j\, \delta\boldsymbol{u}_j + \rho_i\, \delta\boldsymbol{u}_i) \cdot \nabla_i W_{ij}\, V_j \; + \; \mathcal{D}_i^\rho \\[2mm]
\rho_i \dfrac{d\boldsymbol{u}_i}{dt} = -\sum_j (p_j + p_i)\nabla_i W_{ij}\, V_j \; + \; \sum_j (\rho_j\, \boldsymbol{u}_j \otimes \delta\boldsymbol{u}_j + \rho_i\, \boldsymbol{u}_i \otimes \delta\boldsymbol{u}_i) \cdot \nabla_i W_{ij}\, V_j \; + \; \boldsymbol{F}_i^\nu + \rho_i \boldsymbol{g} \\[2mm]
\dfrac{d\boldsymbol{r}_i}{dt} = \boldsymbol{u}_i + \delta\boldsymbol{u}_i, \quad V_i = m_i/\rho_i, \quad p = c_0^2(\rho - \rho_0),
\end{cases}
\tag{33}
$$

where the indexes i and j refer to the generic i-th and j-th particles, $\boldsymbol{F}_i^\nu$ are the viscous forces acting on the particle i, while $\delta\boldsymbol{u}$ is the Particle Shifting velocity adopted to regularize the particles' spatial distribution during their motion. The particle masses m_i are assumed to be constant during their motion. The particles are set initially on a Cartesian lattice with spacing Δr, and hence, the particles' volumes V_i are evaluated initially as Δr^2 and the particle masses m_i are calculated through the initial density field (using the equation of state and the initial pressure field). During the time evolution volumes V_i change in time accordingly with particle density ρ_i. The spatial gradients are approximated through convolution summation with a kernel function W_{ij}. As in [5] a C2-Wendland kernel is adopted in the present work.

The time derivative d/dt used in (33) indicates a quasi-lagrangian derivative, *i.e.*:

$$
\frac{d(\bullet)}{dt} := \frac{\partial(\bullet)}{\partial t} + \nabla(\bullet) \cdot (\boldsymbol{u} + \delta\boldsymbol{u}),
$$

since the particles are moving with the modified velocity $(\boldsymbol{u} + \delta\boldsymbol{u})$ and the above equations are written in an Arbitrary-Lagrangian-Eulerian framework. For this reason the continuity and the momentum equations contain terms with spatial derivatives of $\delta\boldsymbol{u}$ (for details see [6]).

The notation $\boldsymbol{u}_{ji}$ in (33) indicates the differences $(\boldsymbol{u}_j - \boldsymbol{u}_i)$ and the same holds for $\delta\boldsymbol{u}_{ji}$ and $\boldsymbol{r}_{ji}$.

The term $\mathcal{D}_i^\rho$ is the numerical diffusive term introduced by [2] to filter out the spurious high-frequency noise in the pressure field. Following [5] this term is rewritten within an LES framework as follow:

$$
\begin{cases}
\mathcal{D}_i^\rho := \sum_j \delta_{ij}\, \boldsymbol{\psi}_{ji} \cdot \nabla_i W_{ij}\, V_j, \\[3mm]
\boldsymbol{\psi}_{ji} := 2\left[(\rho_j - \rho_i) - \dfrac{1}{2}\left(\langle \nabla\rho \rangle_i^L + \langle \nabla\rho \rangle_j^L \right) \cdot \boldsymbol{r}_{ji} \right] \dfrac{\boldsymbol{r}_{ji}}{\|\boldsymbol{r}_{ji}\|^2} \\[3mm]
\delta_{ij} := 2\, \dfrac{\nu_i^\delta\, \nu_j^\delta}{\nu_i^\delta + \nu_j^\delta}, \qquad \nu_i^\delta := (C_\delta\, l)^2\, \|\mathbb{D}_i\|
\end{cases}
\tag{34}
$$

where C_δ is a dimensionless constant set equal to 6 while $l = 4\Delta r$ is the support of the kernel W and represents the length scale of the filter adopted for the sub-grid model. $\|\mathbb{D}\|$ is a rescaled

Frobenius norm, namely $\|\mathbb{D}\| = \sqrt{2\mathbb{D} : \mathbb{D}}$. The superscript L in (34) indicates that the gradient is evaluated through the renormalized gradient equation, *i.e.*:

$$\langle \nabla \rho \rangle_i^L = \sum_j (\rho_j - \rho_i) \, \mathbb{L}_i^{-1} \, \nabla_i \, W_{ij} \, V_j \,, \qquad \mathbb{L}_i := \left[\sum_k (\boldsymbol{r}_k - \boldsymbol{r}_i) \otimes \nabla_i \, W_{ik} \, V_k \right] \qquad (35)$$

where $\mathbb{L}_i$ is the renormalization matrix (see *e.g* [3]).

The viscous forces $\boldsymbol{F}^v$ are expressed as:

$$\begin{cases} \boldsymbol{F}_i^v := K \sum_j (\mu + \mu_{ij}^T) \, \pi_{ij} \, \nabla_i W_{ij} \, V_j \,, & K := 2(n+2) \,, \\[2ex] \pi_{ij} := \dfrac{\boldsymbol{u}_{ij} \cdot \boldsymbol{r}_{ij}}{\|\boldsymbol{r}_{ji}\|^2} \,, \qquad \mu_{ij}^T := 2 \dfrac{\mu_i^T \, \mu_j^T}{\mu_i^T + \mu_j^T} \,, \quad \mu_i^T := \rho_0 \, (C_S \, l)^2 \, \|\mathbb{D}_i\| \end{cases} \qquad (36)$$

where n is the number of spatial dimensions and C_S is the so called Smagorinsky constant set equal to 0.18 (see [47]). The viscous term (36) contains both the effect of the fluid viscosity μ as well as the one related to the local turbulent viscosity μ_i^T.

Finally, the Particle Shifting velocity $\delta \boldsymbol{u}$ is given by:

$$\begin{cases} \delta \boldsymbol{u}_i^* = -\mathrm{Ma} \, l \, c_0 \sum_j \left[1 + R \left(\dfrac{W_{ij}}{W(\Delta r)} \right)^n \right] \nabla_i W_{ij} V_j \,. \\[2ex] \delta \boldsymbol{u}_i = \min \left(\|\delta \boldsymbol{u}_i^*\|, \dfrac{\max_j \|\boldsymbol{u}_{ij}\|}{2} \right) \dfrac{\delta \boldsymbol{u}_i^*}{\|\delta \boldsymbol{u}_i^*\|} \end{cases} \qquad (37)$$

Here, $\mathrm{Ma} = U_{\max}/c_0$ and the constants R and n are respectively set to 0.2 and 4 as in [41, 50]. The second equation of (37) is introduced to limit the magnitude of the shifting velocity for the purposes of robustness . Since formula (37) is proportional to the smoothing length, the intensity of $\delta \boldsymbol{u}$ reduces as the spatial resolution increases, and this guarantees that $\delta \boldsymbol{u}_i$ induces small deviations with respect to the physical particle trajectory. As documented in [50], the use of the Particle Shifting Technique (PST) leads to regular particle distributions and increases the accuracy and the robustness of the scheme. In turn, the inclusion of the PST causes the loss of the exact conservation of the angular momenta as commented in [50] and in [6].

It is worth noting that the shifting velocity close to the free surface has to be modified to be consistent with the kinematic boundary condition along such an interface. In particular, the normal component of $\delta \boldsymbol{u}$ to the free surface is nullified while the tangential component is maintained unaltered (for more details see [50]).

The system (33) is integrated in time through a 4th-order *Runge-Kutta* scheme. The time step, Δt, is obtained as the minimum over the following bounds:

$$
\begin{cases}
\Delta t_v = 0.125 \min_i \dfrac{(2\Delta r)^2 \rho_i}{(\mu + \mu_i^T)}, \quad \Delta t_a = 0.5 \min_i \sqrt{\dfrac{2\Delta r}{\|\boldsymbol{a}_i\|}}, \quad \Delta t_c = 1.5 \left(\dfrac{2\Delta r}{c_0}\right), \\[4mm]
\Delta t = \min(\Delta t_v, \Delta t_a, \Delta t_c)
\end{cases}
\tag{38}
$$

where $\|\boldsymbol{a}_i\|$ is the particle acceleration and Courant-Friedrichs-Lewy constants are set for the adopted kernel (C2-Wendland kernel). For the cases studied in this work the second two constraints are always the most critical.

VI.   ENERGY DISSIPATION WITHIN THE δ-LES-SPH MODEL

Following the analysis performed in [4] and in [39] the energy balance for the particle system can be extended to the δ-LES-SPH equation presented in the previous section. For the sake of brevity only the main terms are briefly reported in this section. The δ-LES-SPH energy balance can be written as:

$$
\dot{\mathcal{E}}_M + \dot{\mathcal{E}}_C = \mathcal{P}_V + \mathcal{P}_V^{turb} + \mathcal{P}_N + \mathcal{P}_{ext}, \qquad \mathcal{P}_N := \mathcal{P}_\delta + \mathcal{P}(\delta\boldsymbol{u})
\tag{39}
$$

where $\mathcal{E}_M$ is the mechanical energy of the particle system, composed of kinetic energy $\mathcal{E}_K = \frac{1}{2}\sum_i m_i \|\boldsymbol{u}_i\|^2$ and potential energy $\mathcal{E}_P = \sum_i m_i g y_i$ whereas $\mathcal{E}_C$ is the elastic potential energy (12) in which the integral is rewritten as a sum over the fluid particles. The external power $\mathcal{P}_{ext}$ due to the tank motion is evaluated through the mutual interaction between fluid and solid particles, as detailed in [4] and [11]. Following the latter, the power terms related to the viscous forces in particles interactions are given by:

$$
\mathcal{P}_V = \mu \frac{K}{2} \sum_i \sum_j \pi_{ij}\, \boldsymbol{u}_{ij} \cdot \nabla_i W_{ij}\, V_i\, V_j, \quad \mathcal{P}_V^{turb} = \frac{K}{2} \sum_i \sum_j \mu_{ij}^T \pi_{ij}\, \boldsymbol{u}_{ij} \cdot \nabla_i W_{ij}\, V_i\, V_j
\tag{40}
$$

Finally, the term $\mathcal{P}_N$ takes into account the effect of the density diffusion $\mathcal{P}_\delta$ (see [39]):

$$
\mathcal{P}_\delta = \frac{\delta c_0 h}{2} \sum_i \sum_j \left(\frac{p_j}{\rho_j} - \frac{p_i}{\rho_i}\right) \boldsymbol{\psi}_{ij} \cdot \nabla_i W_{ij}\, V_i\, V_j,
\tag{41}
$$

and the term related to the particles shifting $\delta\boldsymbol{u}$, *i.e* $\mathcal{P}(\delta\boldsymbol{u})$. Both these two terms are related to the stability of the scheme and are collected together in $\mathcal{P}_N$ as a numerical diffusive term. Following

19

Eq. (28) the discrete form of the energy dissipated, $\mathcal{E}_{diss}$, can be expressed as:

$$\mathcal{E}_{diss} = \int_{t_0}^{t} \mathcal{P}_{diss}\, dt, \qquad \mathcal{P}_{diss} := \mathcal{P}_V + \mathcal{P}_V^{turb} + \mathcal{P}_N. \tag{42}$$

As discussed in [35], during liquid impacts energy losses occur. As already mentioned in section III C, the weakly-compressible assumption underlying our scheme implies that during impacts, a portion of the mechanical energy is converted into internal compressible energy in the form of acoustic waves, and then is mainly dissipated by numerical diffusive terms, *i.e.* the $\mathcal{P}_{\delta}$ term. Therefore, as shown in [39], the energy lost in liquid impacts is represented by the $\mathcal{P}_N$ component. That numerical dissipation, however, becomes less important with respect to viscous dissipation ($\mathcal{P}_V + \mathcal{P}_V^{turb}$) when impacts are not occurring and vortical structures are generated during the post-impact events.

When increasing the spatial resolution both $\mathcal{P}_N$ and $\mathcal{P}_V^{turb}$ decrease while the fluid viscosity component $\mathcal{P}_V$ increases, as more and more small scales of the velocity gradient (*i.e.* shock waves and small vortexes) are resolved. As suggested in [44] in a well resolved LES simulation the resolved turbulent kinetic energy should be greater than the modelled energy. Therefore, the power associated with fluid viscosity $\mathcal{P}_V$ (which depends upon the resolved velocity gradients) should be greater than $\mathcal{P}_N$ and $\mathcal{P}_V^{turb}$. These aspects will be discussed in the next section.

It is worth noting that even in the discrete form $\mathcal{E}_C$, $\mathcal{P}_V$, $\mathcal{P}_V^{turb}$ and $\mathcal{P}_{\delta}$ are invariant when evaluating them in the I-FoR or in the Ni-FoR.

VII.   RESULTS: SLOSHING IN FORCED PERIODIC HEAVE MOTION

In this section the problem described in Sec. II is addressed. Due to continuous energy fluxes exchanged between the solid and the fluid in the coupled system in question, the evaluation of the energy dissipated by the fluid is particularly complex. Therefore, in the present work we simplify the problem by studying the sloshing flow obtained by a purely harmonic imposed motion. In this way we can estimate the energy dissipation rate across a period and study its long term behaviour. Conversely, in in the second part of this paper (Part II) the problem will be studied using the actual acceleration time history recorded in the experiments by [37], which exhibits a rapid decay of the tank motion. It is important to underline here that the approach followed in the analysis of the numerical results has to take into account the turbulent and chaotic nature of the problem. In order to address this relevant aspect a stochastic approach has been required to corroborate our findings.

As described in Sec. II, when the fluid is at rest two menisci are present close to the vertical walls because of the surface tension. In order to include this effect in the simulation, those menisci are numerically replicated in the initial conditions (see inset in the left plot of Fig. 1) by adding, close to the vertical boundaries, a small fluid triangle forming an angle of contact of $\theta = 45°$, which is the one corresponding to the water surface tension.

The tank is subjected to a purely harmonic vertical motion following the law: $y(t) = -A\cos(\omega t)$, with $\omega = 14\pi \, rad/s$ and the motion amplitude $2A/L = 2.068$. The flow is also subjected to gravity acceleration. Since $\omega^2 A/g = 20.4$ the flow is driven by inertia and is always in the regime of "shaken flow", as defined in the introduction. In the present test case the vertical acceleration ratio $\omega^2 A/g$ has been doubled with respect to the experiments in [37]. This choice is motivated by the need of representing an energetic wind gust, similarly to what was done in the experiments in [53].

The maximum tank velocity is equal to $U_{max} = \omega A = 4.55$ m/s and the speed of sound is set equal to $c_0 = 8.8\omega A = 40 m/s$; it will be shown that this value is high enough to guarantee the weakly-compressible regime. The numerical resolution adopted for the discussion in sections VII A and VII B, is $N = H/\Delta r = 200$ and the time history covers 140 periods of oscillation. Note that the Reynolds number of the simulation is Re=455,000. For this value, the ratio between H and the boundary layer thickness, estimated through Blasius equation, is expected to be $O(10^3)$. Therefore, even for the maximum spatial resolution considered, it is not possible to resolve the boundary layer for this test case and a free-slip boundary condition is preferred, as already discussed in Sec. III A.

Throughout the present section the dissipated energy, $\mathcal{E}_{diss}$ (42), is made non-dimensional by the potential energy $\Delta\mathcal{E} = \rho L H g 2A = 6.086 \, J$, corresponding to a power in one cycle equal to $\Delta\mathcal{P} = \Delta\mathcal{E}/T = 42.48 \, W$. The latter is used to make the time variation of the dissipated energy non-dimensional.

A. Short time evolution: description of the dissipative mechanism

Here the different stages of the flow evolution are described: plots from a) to f) of Fig. 2 show the flow configuration in some key instants; contour fields refer to the value of the ratio of the turbulent viscosity over the fluid viscosity μ_T/μ (see Eq. 36). Regions of the flow where μ_T/μ is higher are representative of a higher level of local energy dissipation. In Fig. 3 the dissipated energy $\mathcal{E}_{diss}$ is plotted together with the tank motion in order to clearly show the relation between

flow motion and tank oscillation. In the same figure the flow instants depicted in Fig. 2 are indicated by means of their respective labels.

In the initial stage, during the first upward acceleration of the tank, a small free-surface wave is generated due to the rupturing of the menisci at the lateral walls. The waves travel from the lateral walls towards the center of the tank. At t/T=0.25, when the acceleration changes sign, those small free-surface perturbations become the triggering points from which the Rayleigh-Taylor instability develops (plots (a) and (b) of Fig. 2). The fluid is accelerated upwards and two main jets detach from the free-surface, eventually impacting against the tank ceiling (plot (c) of Fig. 2). The flow evolution does not imply any relevant loss of the mechanical energy until the impact at $t/T = 0.56$, as highlighted by the low levels of μ_T/μ and as also confirmed in Fig. 3. However, when the impact occurs a relevant amount of energy is suddenly dissipated (point (d) on the curve).

This energy loss is mostly due to the generation of acoustic waves at the contact line between the free surface and the wall (with dissipation mechanisms similar to those described in [35]) and to the generation of high vorticity due to multiple reconnections of the fluid jets. Indeed, as shown in Fig. 3 (d) higher levels of μ_T/μ are observed in the region close to the ceiling. Here, the violent flow resulting from the impact generates large velocity gradients which correspond to intense turbulent stresses, and consequently, to a large amount of energy dissipated in this region.

After this stage, at $t/T = 0.75$ the tank acceleration changes sign again and the fluid is ejected in the opposite direction. However, differently from the first ceiling impact, this time the solid bottom is already covered with a large amount of liquid which has flowed during the first impact. The impact is less violent, but occurs with a larger generation of vorticity due to the multiple liquid-liquid impacts (Fig. 2 (e)). This reflects in a larger loss of energy with respect to the first impact, as a larger amount of liquid is involved. After that, another cycle starts: the flow impacts against the ceiling (Fig. 2 (f)), then against the bottom and so forth. During the fluid evolution, local high values of μ_T/μ are recorded (up to μ_T/μ =25). These large values indicate that the spatial resolution is not fine enough for a proper LES modelling of the flow (see, *e.g.*, [17]). This aspect is further inspected below when analysing the different components of the energy dissipation.

In the left plot of Fig. 4 the vorticity contour at $t/T = 0.98$, corresponding to plot e) of Fig. 2, is depicted. From this plot it is possible to identify the main size of the eddies resolved in the numerical simulation. In the right plot of the same figure the contour plot of the vertical component of the velocity field is reported for $t/T = 0.56$, that is, when the liquid jets are fully developed. Note that the velocity field here is reported in the Ni-FoR, that is, deducting the velocity of the
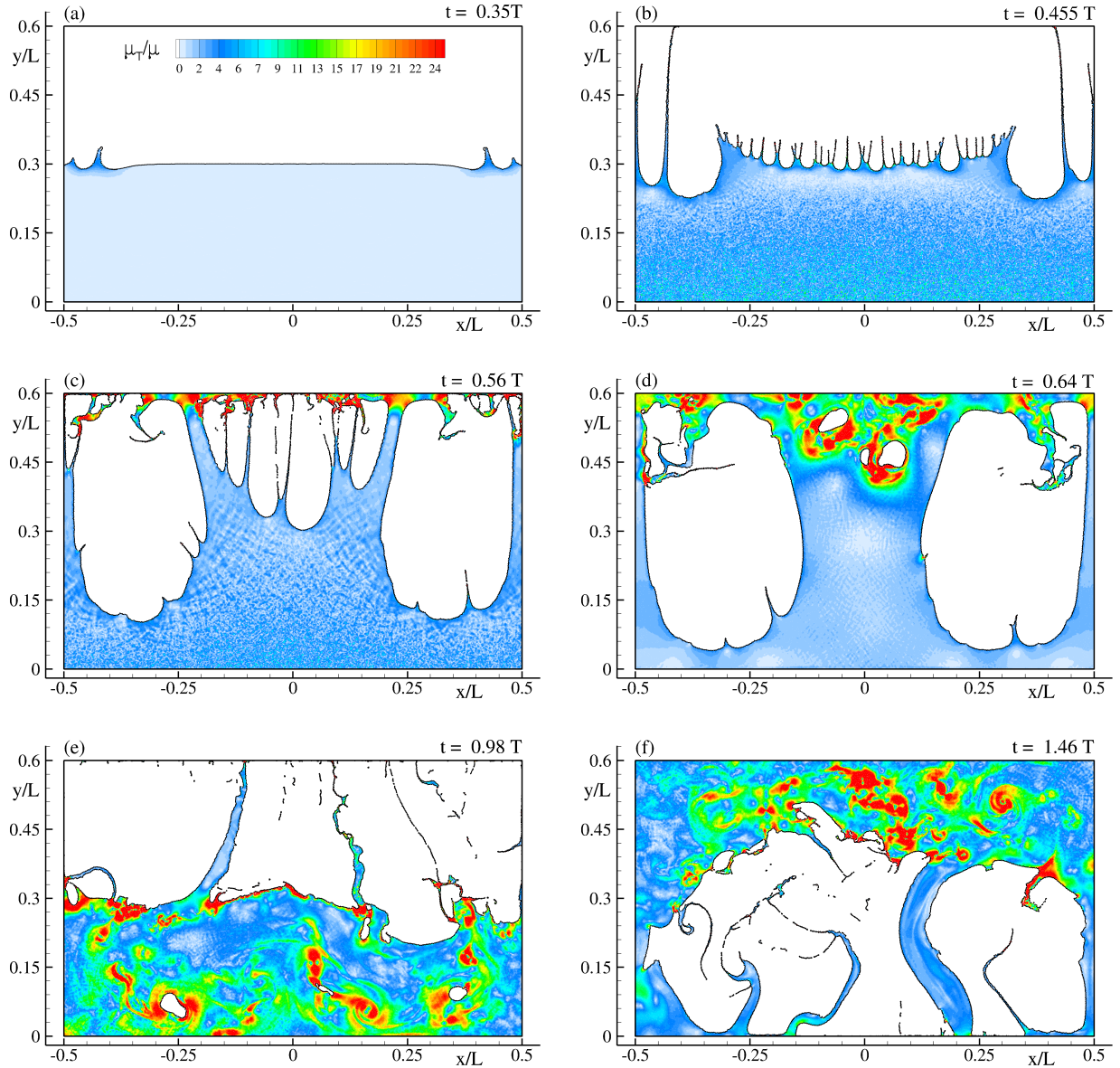
FIG. 2: Flow evolution in the forced harmonic heave motion obtained by δ-LES-SPH. Colors refer to the ratio μ_T/μ. Plot sequence is from top to bottom and from left to right. Spatial resolution $N = 200$.

tank. According to the highest values displayed, the choice of the speed of sound verifies the assumption of weak compressibility. This will also be confirmed later on when analysing the pressure values.
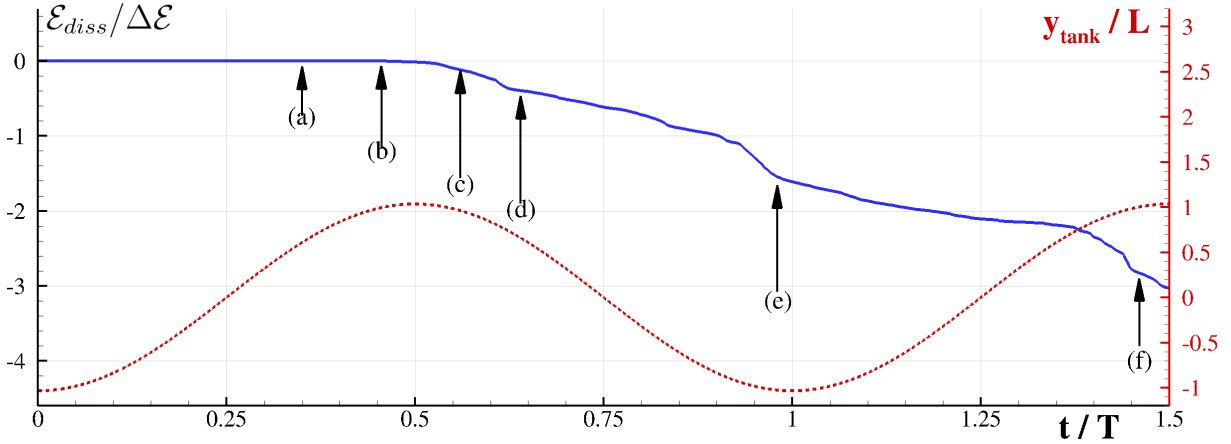
FIG. 3: Dissipated energy $\mathcal{E}_{diss}$ (solid line) and corresponding tank elevation (dashed line). Labels (a) to (f) are related to plots of Fig. 2.
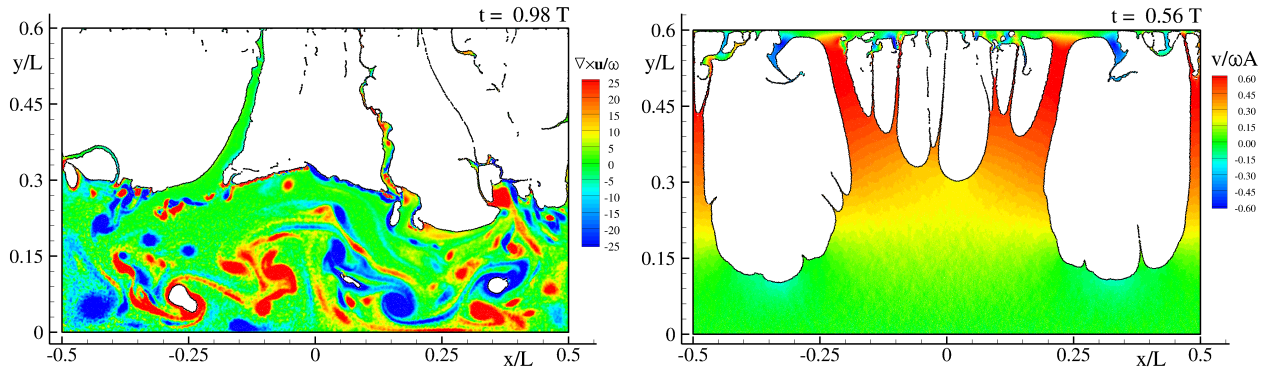
FIG. 4: Left: vorticity contour at $t/T = 0.98$, corresponding to plot e) of Fig. 2. Right: contour plot of the vertical component of the velocity field at $t/T = 0.56$ corresponding to plot c) of Fig. 2.

B. Short time evolution: comparison between δ-LES-SPH model and standard SPH-LES model

In order to justify the adoption of a complex model such as the one described in Sec. V the same test has been repeated by using a classical SPH scheme (Monaghan 1994) with LES modelling by Dalrymple and Rogers (2006) (which hereinafter will be denoted as "LES-SPH"). In Fig. 5 the obtained initial flow evolution is depicted for the same time instants as in Fig. 2 labels (b), (c), (d), (e). Due to the absence of a tensile instability control in the scheme, the intense negative pressure in the fluid, resulting after the inversion of the acceleration direction at t/T=0.25 causes the fluid to numerically cavitate and the particles to separate from the bottom wall at t/T=0.385 (Fig. 5 (b')).

24
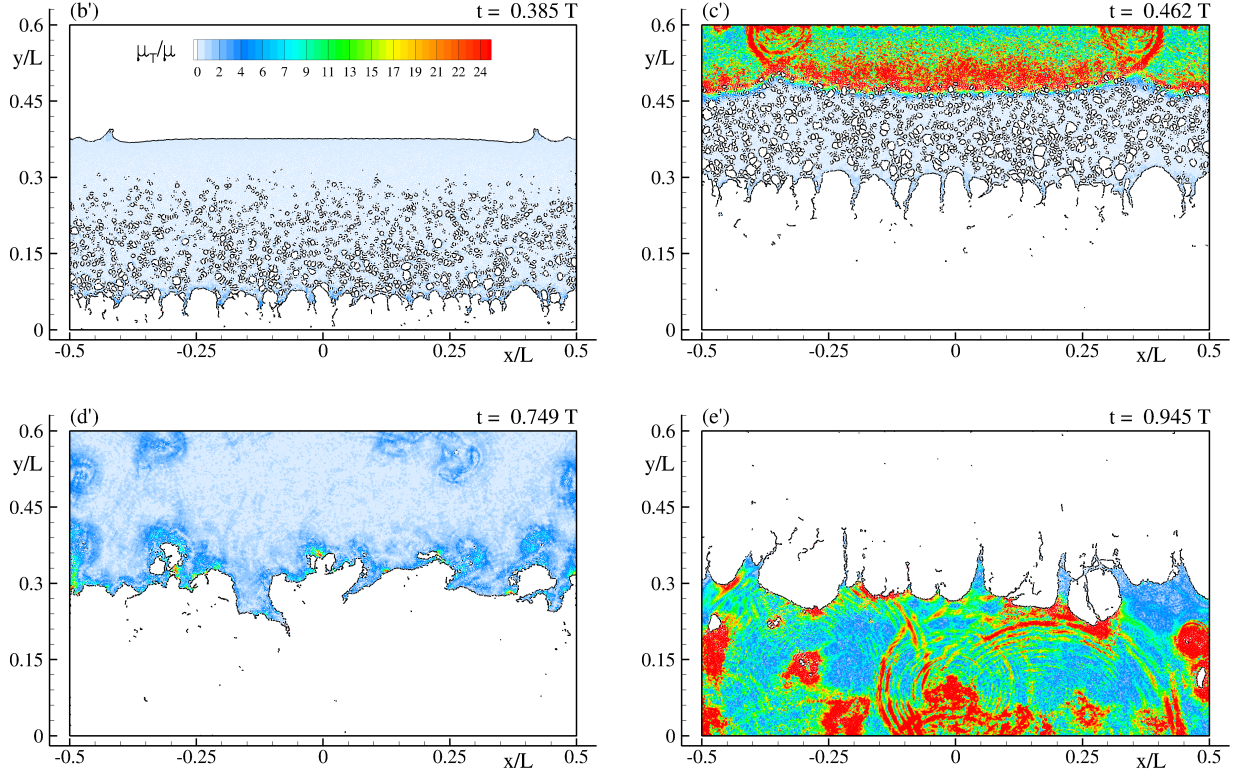
FIG. 5: Flow evolution obtained by LES-SPH. Colors refer to the ratio μ_T/μ. Plot sequence is from top to bottom and from left to right. Spatial resolution $N = 200$.

As a consequence, the fluid detaches as a compact fluid block from the tank bottom and is ejected towards the ceiling, eventually impacting against the wall.

It is worth remarking that the negative pressure at which the numerical cavitation occurs is far from the suction pressure which would cause an actual physical cavitation in the liquid. Indeed, assuming the maximum suction pressure to take place at the acceleration peak, in the experimental scale it results $|P_{max}| = \rho(\omega^2 A - g)H \simeq 6$ kPa which is at least one order of magnitude smaller than the one needed to reach vapour pressure at an ambient temperature of 20°C.

At the impact (Fig. 5 (c')) the free surface is almost parallel to the wall. In this configuration a flat impact evolution is expected as described in [35] and a water hammer pressure can develop in the impact region generating a shock front. A large amount of kinetic energy is instantaneously converted into internal compressible energy $\mathcal{E}_C$ in the form of acoustic waves. These acoustic waves are then dissipated by the numerical diffusion of the solver, which results in a corresponding loss of mechanical energy. After the acoustic waves are dissipated, no significant velocity gradients are observed (Fig. 5 d')) because the flow has lost a large part of its mechanical energy.
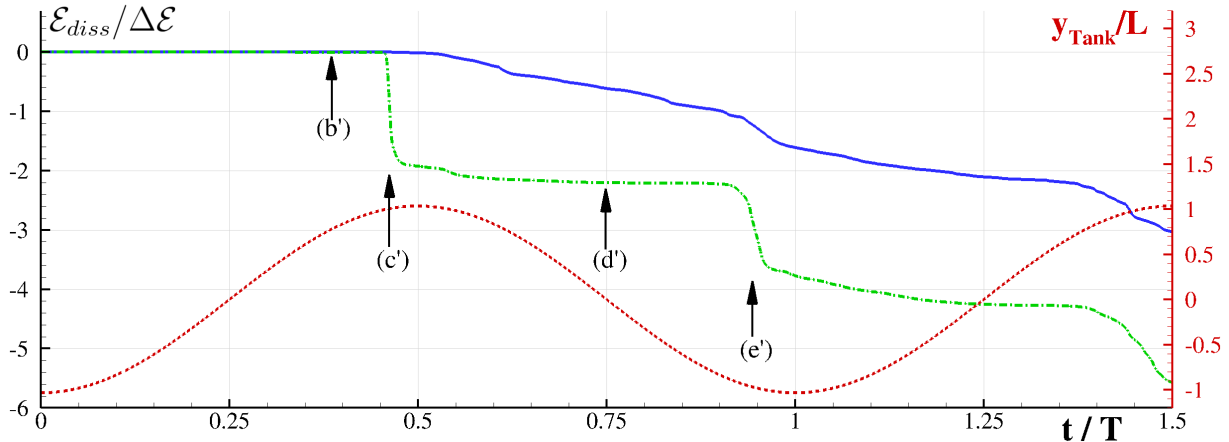
FIG. 6: Comparison of the energy dissipated in the LES-SPH scheme (dash-dotted line) and in the present δ-LES-SPH scheme (solid line). The dashed line indicates the tank elevation. Labels (b') to (e') are related to plots of Fig. 5.

This is also clearly visible in Fig. 6 where the energy dissipated in the LES-SPH scheme is compared to that obtained by the present δ-LES-SPH scheme. At t/T=0.462 (label (c')) a large and sudden decrease of the energy is observed in the curve by the standard SPH whereas the δ-LES-SPH exhibits only an initial slow energy decay. The behaviour of the standard SPH closely resembles the instantaneous energy drop observed in flat impacts as described in [35]. After that, the absence of intense velocity gradients results in a plateau of the energy which persists up to the next impact. In the subsequent evolution the flow becomes more complex and the free surface is no longer parallel to the wall at the impact time (Fig. 5 (d) and (e)). Therefore the acoustic waves are not generated in a single shock front, but are rather produced sparsely at each free-surface contact point. The resulting energy drop, with respect to the first one, is less intense but equally steep. In Fig. 7 the pressure measured at the upper-left corner of the tank is shown for the δ-LES-SPH schemes. The measured pressure is generally well below the "weakly-compressible limit" given by the eq (4), thus confirming the validity of the weak compressibility assumption.

As a further general comment, from plot (c') and (e') we observe that high values of μ_T/μ are distributed on shock waves generated during fluid-wall (plot (c')) and fluid-fluid (plot (e')) impacts. This is an unphysical way of working for the LES model, and in the LES-SPH scheme is consequent to the absence of a numerical mechanism for introducing dissipation in high density gradients. As such, the needed numerical dissipation is introduced by the LES model which is, however, beyond the scope of its design. This is a further indication of the inappropriateness of
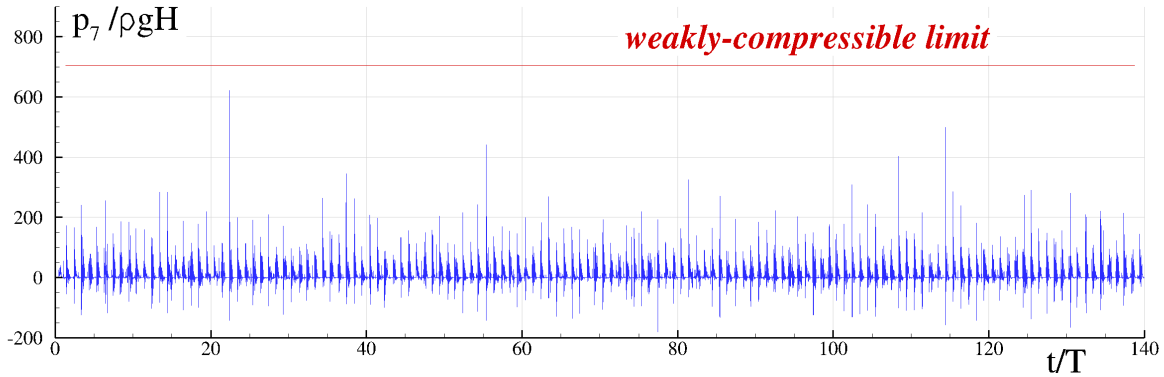
26

FIG. 7: Pressure measured at the top-left corner of the tank. The red solid line represents the "weakly-compressible limit" given by the eq (4) . Top plot: comparison between δ-LES-SPH scheme (solid line) and LES-SPH scheme (dashed line) for the time range [0:4] t/T. Bottom plot: pressure recorded throughout the entire δ-LES-SPH simulation.

the LES-SPH scheme for modelling this flow.

Conversely, in the δ-LES-SPH scheme the dissipation in acoustic waves is handled by the diffusive term in the continuity equation (34) and essentially the LES filtering acts in turbulent regions of the flow.

C. A simple analytical dissipation model

As a further term of comparison the solutions from purely inelastic analytical model are reported in the same figure. The analytical model is similar to the ballistic model as described in [15] and has been derived by assuming the following simplifications:

- the problem is studied in 1D, i.e. only in the vertical direction;

- the gravity acceleration is neglected;

- the water is free to detach from the boundary without any suction effect as soon as the pressure at the wall becomes negative;

- after the detachment the fluid patch follows its ballistic trajectory with constant velocity equal to the tank velocity at the time of the detachment;

27
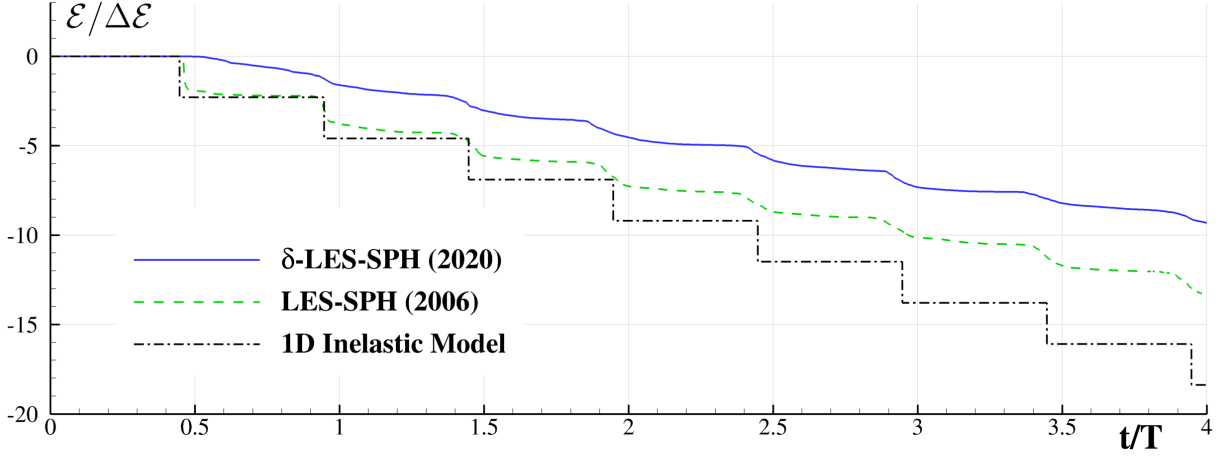
FIG. 8: Comparison of the energy dissipated in the LES-SPH scheme (dashed line), in the present δ-LES-SPH scheme (solid line) and in the 1D analytical model (dash-dotted line).

- the impact with the wall is purely inelastic: when the fluid patch impacts the tank wall it instantaneously loses all its kinetic energy;

The interested reader can find more details about the governing equations in [15]. The resulting flow is periodic, having the same period as the tank motion. The extreme simplifications above allow drawing the system energy evolution by simply studying the law of motion of the tank. Impacts occur at $t^* = T/4 + kT/2 + 0.196T$ where $k \in N$, and cause a steep reduction in the system energy of about $\mathcal{E}_{diss}/\Delta\mathcal{E} = -2.3$ (considering that at $t = t^*$ the relative velocity between the fluid block and the tank is $v_{rel} = 0.67\omega A$).

The obtained energy curve is the black stepped line represented in Fig. 8: it is far from representative of the energy dissipation in the actual physical system, but it is useful as it shows a lower boundary of the system energy. In Fig. 8 it can be also observed that the first energy step in the standard SPH model is very close to the one predicted by the 1D model in terms of time and energy lost. Then, as the flow loses its compact shape in the subsequent impacts, the behaviour of the energy decay gradually changes its sharp-edge, stepped aspect and becomes more similar to the δ-LES-SPH solution.

D. Mid time evolution: description of the dissipative mechanism

After the initial transient the flow reaches a quasi-periodic regime characterised by a stepped aspect of the energy curve. For each period of the motion law, two energy steps occur which
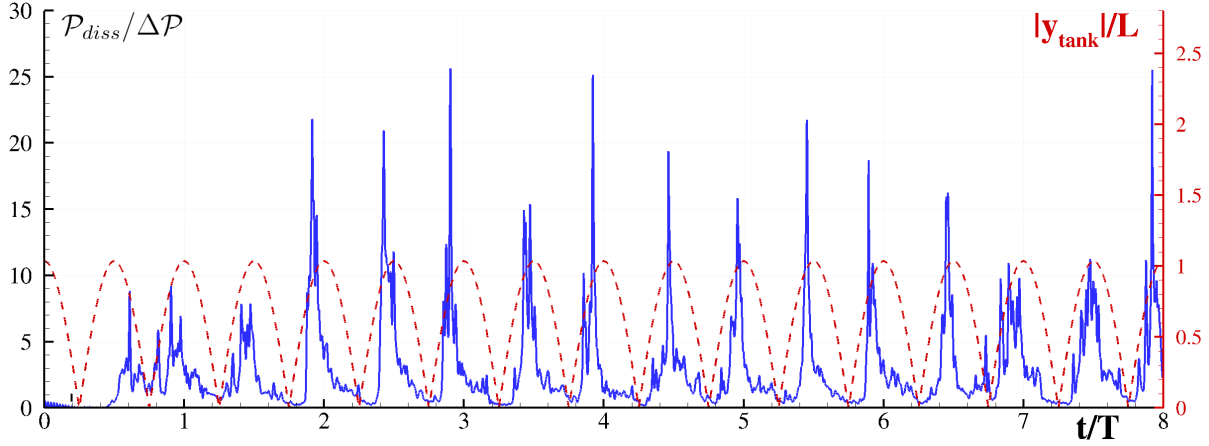
28

FIG. 9: Time history of the non-dimensional time derivative of the dissipated energy, $\mathcal{P}_{diss}/\Delta\mathcal{P}$ (solid line) and of the absolute value of the tank displacement (dashed line).
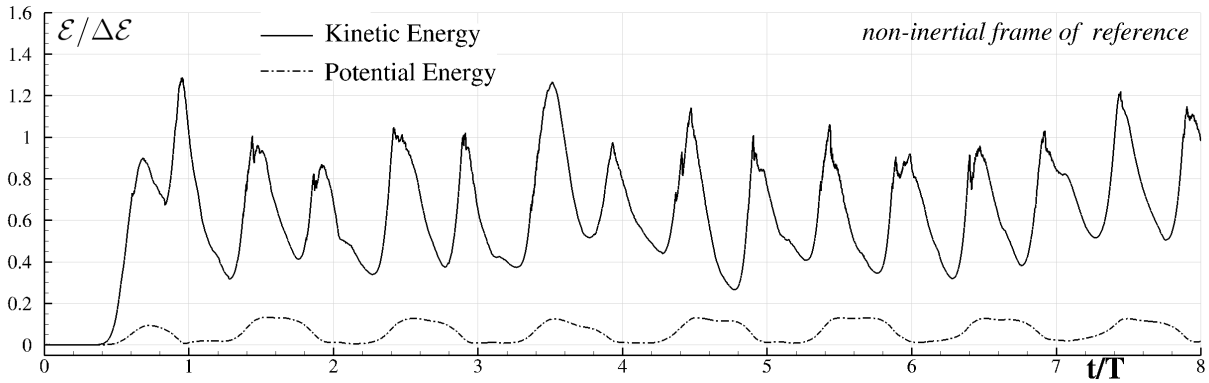

FIG. 10: Time history of the kinetic energy $\mathcal{E}_K$ (solid line) and of the potential energy $\mathcal{E}_P$ (dashed line) in the Ni-FoR.

are characterised by phase-shifts almost constant with respect to the tank motion. Each energy loss takes place after the tank velocity maximum, but before the tank reaches the extremal displacement. This can be clearly seen in Fig. 9 where the absolute value of the tank displacement is plotted against the time derivative of the dissipated energy, $\mathcal{P}_{diss}/\Delta\mathcal{P}$. In most of the occurrences, in each half-period the peak of the dissipation rate occurs just before the tank reaches its extremal value and then rapidly decays. This can be explained by the fact that the fluid impacts the opposite wall before the tank actually stops and changes its direction of motion.

In Fig. 10 only kinetic and potential energy components of the fluid are reported for the first 8 periods of oscillation. These quantities are here computed in the Ni-FoR in order to analyse the fluid energy content devoid of the contribution related to the tank motion. As expected, the kinetic

energy is dominant to the potential energy, but both follow the oscillation frequency imposed by the tank movement. Apart from that, this plot is useful in getting an estimation of the relevant turbulent length scales by evaluating the turbulent kinetic energy content and its rate of decay [30]. To this end, we need to estimate the turbulent kinetic energy per unit mass k and the rate of energy dissipation per unit mass ϵ. An estimation of k can be obtained from Fig. 10 which corresponds to the kinetic energy in the non-inertial frame of reference (in our case the fluid is assumed to be fully turbulent), while ϵ can be estimated from Fig. 9. From those plots we obtain $k\,M/\Delta\mathcal{E} \approx 0.7$ and $\epsilon\,M/\Delta\mathcal{P} \approx 10$ as representative values of the flow in the stage after the impact, where intense mixing occurs and energy is dissipated due to the high velocity gradients.

The scale of the large energetic eddies can be evaluated as

$$l \approx \frac{k^{3/2}}{\epsilon} \tag{43}$$

and using the above values of k and ϵ we get $l/H \approx 1$. As expected the large eddies have a size comparable with the filling height.

The Taylor microscale λ is the length scale below which viscous effects become relevant in the flow evolution, demarcating the inertial subrange. This length scale is important in LES modelling since the adopted spatial filter should be at least smaller than λ in order to resolve the main turbulent eddies (see [44]). The Taylor microscale λ can be evaluated as:

$$\lambda \approx \sqrt{10\,\nu\,k/\epsilon} \tag{44}$$

where ν is the fluid kinematic viscosity. The obtained value for the Taylor microscale λ at this stage is $\lambda/L \approx 4 \cdot 10^{-3}$ which corresponds to $H/\lambda \approx 100$. Therefore, a resolution $N = H/\Delta r \approx 200$ could be sufficient for the LES model to be correctly applied, since the spatial filter lies below the Taylor microscale. However, as shown below in the analysis of the energy components, a further increase of the resolution is needed.

A proof of the above estimation is given in figure 11 where the vorticity field at time $t = 1.25T$ is depicted using a very high spatial resolution, namely $H/\Delta r = 800$. On the right plot of the same figure a zoom of the field is depicted comparing the vortex scales with the Taylor microscale estimated above. At this resolution most of the vortices contain enough particles which means that the inertial scale is well resolved and that, at this discretization level, we are approaching a Direct Numerical Simulation (DNS).

Indeed, applying the same reasoning to evaluating the Kolmogorov microscale, we can estimate
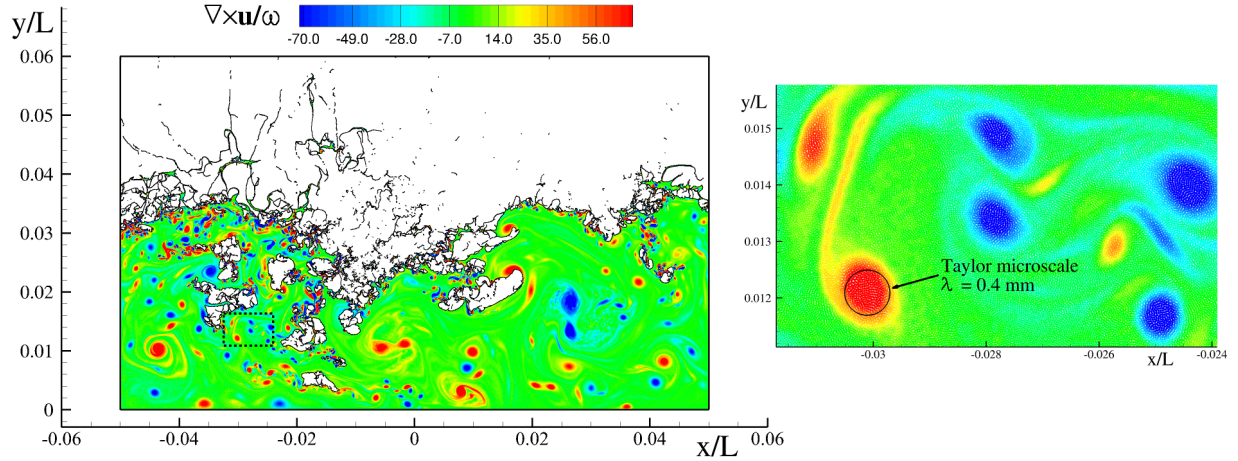
30

FIG. 11: SPH vorticity field at $t/T = 1.25$ using a spatial resolution $N = 800$. On the right plot an enlargement of the field is depicted comparing the vortexes size with the evaluated Taylor microscale.

it as:

$$\eta \approx (\nu^3/\epsilon)^{1/4} \tag{45}$$

which gives $\eta/L \approx 10^{-4}$ and $H/\eta = 3,000$. The latter represents a rough estimate of the needed resolution in order to resolve all the viscous length scales of the flow, i.e., to perform a DNS. The present numerical simulations are therefore far from being a DNS for which the needed computational cost would be about 10,000 times larger than the case at $N = 100$ which is used in the following for performing the statistical analysis.
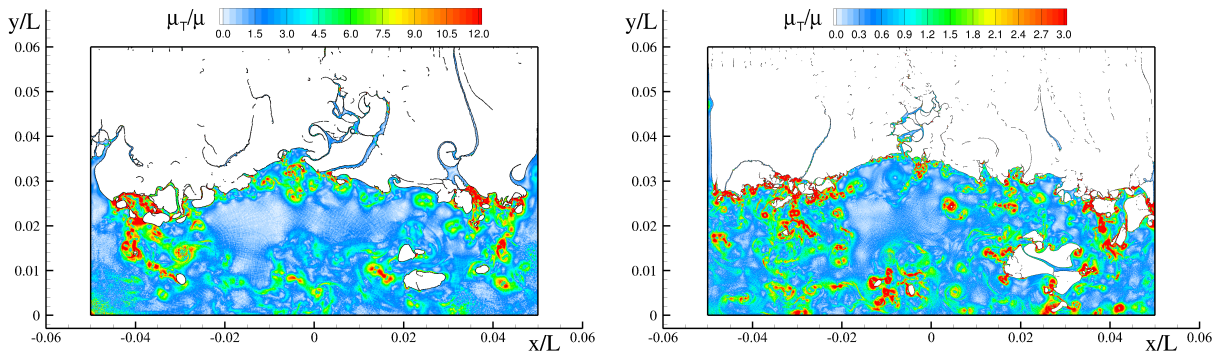
FIG. 12: SPH turbulent viscosity μ_T field at $t/T = 0.98$ using a spatial resolution $N = 400$ (left) and $N = 800$ (right).

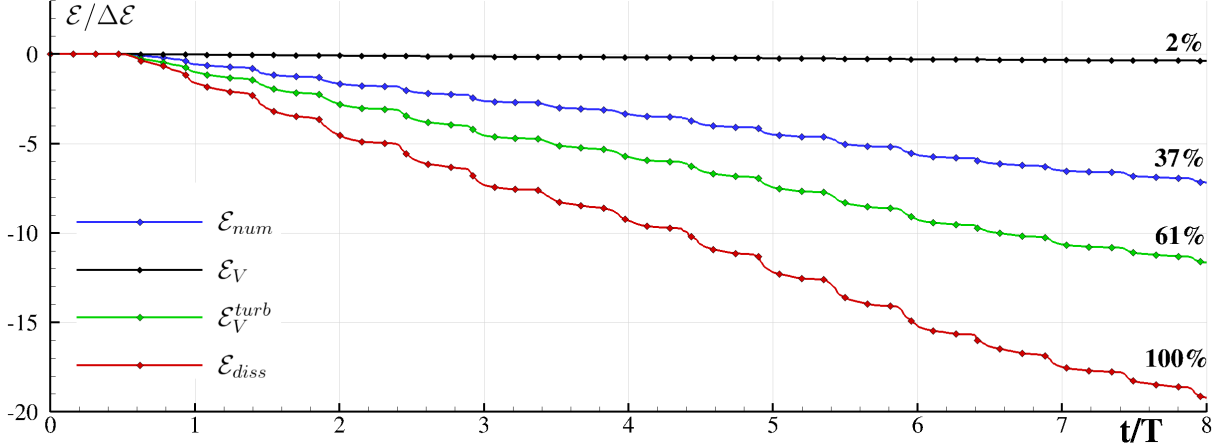In Fig. 12 the ratio μ_T/μ is depicted at time $t = 0.98T$ using two spatial resolution $N = 400$ and

31

FIG. 13: Time history of the energy components defined in section VI: resolved viscous dissipation $\mathcal{E}_V$, modelled turbulent viscous dissipation $\mathcal{E}_V^{turb}$, numerical diffusion $\mathcal{E}_N$, total energy dissipation $\mathcal{E}_{diss}$. Spatial Resolution is $N = 200$.

$N = 800$. Comparing those two plots with the one of Fig. 2 is it possible to appreciate how the turbulent viscosity decreases in magnitude using larger spatial resolution. In particular at N=800 where the inertial scale is well resolved the ratio μ_T/μ remain of order $O(1)$.

In order to better understand the energy dissipation mechanisms acting in the δ-LES-SPH, in Fig. 13 the different energy components defined in Sec. VI namely $\mathcal{E}_V$, $\mathcal{E}_V^{turb}$, $\mathcal{E}_N$ (which are the time integrals of their corresponding power terms) are plotted against time. The modelled turbulent viscous dissipation $\mathcal{E}_V^{turb}$ is the most prominent term among the others, and after 8 periods of oscillation, contributes to 61% of the total energy dissipation. It acts continuously exhibiting higher intensity during liquid impacts, and its action is related to the large velocity gradients developed in the flow. The numerical term, $\mathcal{E}_N$, is the second one contributing to 37% of the total dissipation after 8 periods. It exhibits a more pronounced stepped trend with clear plateaus between one step and the following one. This is due to the nature of this term which acts mostly on steep gradients of the density fields. Indeed, due to the strong shock waves generated during liquid collisions, a large amount of energy is dissipated in a short time during the periodic impacts occurring in the tank. As shown in [39], when increasing either the spatial resolution or the viscosity, the $\mathcal{E}_N$ term becomes less important.

As for the viscous dissipation, this term is practically negligible with respect to the other components, the spatial resolution not being fine enough. As already mentioned, this means that the spatial discretization should be further increased in order to have a proper LES modeling of

the flow. This is not feasible for the present test case due to the very long time history involved. However, in the second part of this paper (Part II), where the numerical simulation is compared with experimental data, the spatial resolution is pushed up to $N = 400$ in order to produce a finer representation of the main eddies and smaller values of μ_T/μ.

E. Long time evolution: linear decay of the dissipated energy

In Fig. 14 the energy decay is shown for the entire simulation duration, that is, 140 periods of oscillation. In the same plot the energy curve is fitted through a linear regression. The related coefficient of determination, R^2, is defined as:

$$R^2 = 1 - \sum_i (\mathcal{E}_i - \bar{\mathcal{E}})^2/(\mathcal{E}_i - y_i)^2 \qquad (46)$$

where $\bar{\mathcal{E}}$ is the time average of the energy computed on the whole time history, and $\mathcal{E}_i$ and y_i are, respectively, the i-th values of the time history of the energy and of the fitted line. R^2 for this test is equal to 0.999927 or $(1 - R^2) = 7.3\,10^{-5}$. The result is that the energy dissipation is well represented by a linear approximation, and at this time scale, the dissipation rate is almost constant throughout the entire history and is equal to $\bar{\mathcal{P}}_{diss}/\Delta\mathcal{P} = 2.906$. This suggests that, apart from the specific flow configuration in the single impact, which is different for all the events, the amount of energy lost is generally almost constant.

In Fig. 15 the energy curve has been plotted again removing the linear component shown above. It can be observed that a high-frequency saw-tooth component is present (inset in the figure). This
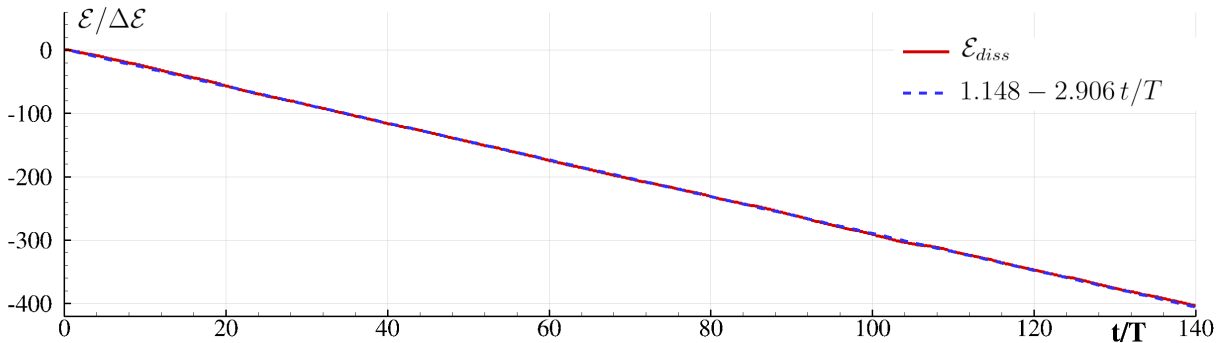

FIG. 14: Energy dissipation over the simulation time duration. that is, 140 periods of oscillation. The solid line represents the raw simulation data, whereas with the dashed line the related regression line is drawn.
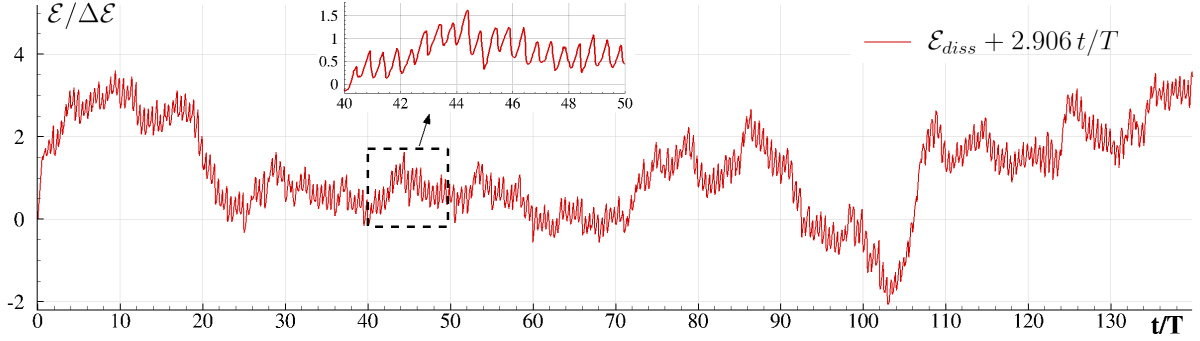
FIG. 15: History of the energy dissipation without of its linear component $\bar{\mathcal{P}} t = -2.906 \, t$.

component accounts for each single energy drop following a liquid impact of the fluid against either the roof or the bottom, and in agreement with Fig. 9, has a frequency which is twice that of the motion frequency. On the other hand, a rather chaotic component acting on a larger time-scale (order of 10-20 time periods) is observed.

Across a few time periods, the complex flow dynamics inside the tank can cause local flow features which can have consequences on the flow for several cycles. This behaviour reflects the chaotic nature of the problem, the flow being fully turbulent. In the next subsection this complex behaviour is investigated in terms of stochastic analysis through a series of simulations.

F. Repeatability of the simulations

In order to study the repeatability character of the numerical simulation, a stochastic approach has been followed. The same simulation has been repeated 10 times by introducing a small random disturbance - of the order of 1% of the particle size - on the initial particle lattice. The applied noise is represented in Fig. 16 and compared to a perfect cartesian lattice and a noise of 10% of the particle size. This tiny disturbance has the sole role of emphasizing and anticipating the comparison of chaotic behaviour in the numerical simulation. In order to reduce the computational effort for such a study the resolution adopted has been decreased to $N = 100$. However, it is important to note that due to the large computational costs involved, the present analysis is not meant to be a statistical characterization of the flow. The whole domain is indeed too small to allow drawing any sound conclusion from a statistical point of view, the latter being out of the scope of the present paper.

In Table I the dissipation rate $\bar{\mathcal{P}}/\Delta\mathcal{P}$ obtained computing the steepness of the regression line is
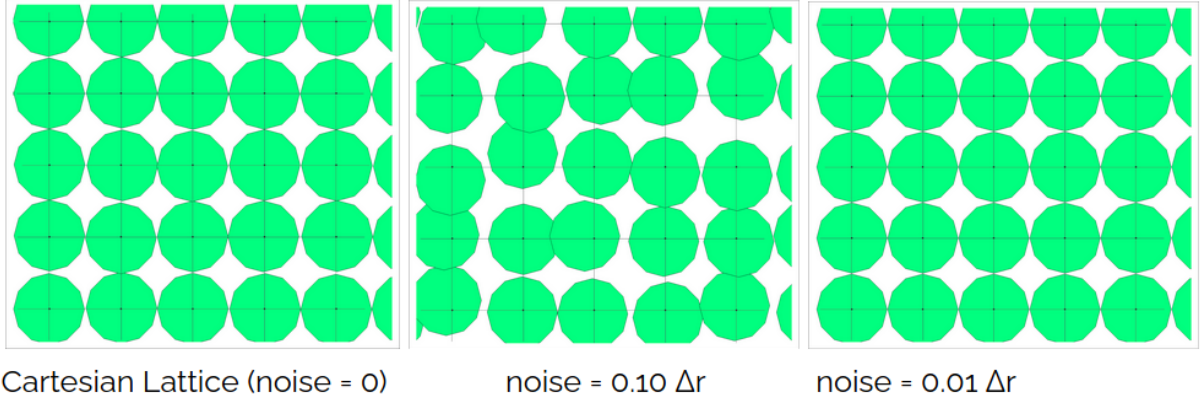
34

FIG. 16: Sketch of different levels of random noise applied on the initial particle lattice. The right plot shows the 1% noise configuration adopted for the simulations.

reported for each of the 10 repetitions of the numerical simulation. In the same table the accuracy of the regression is also reported and expressed, for ease of reading, as $(1 - R^2) \times 10^5$. The same is also evaluated for the ensemble average curve computed as:

$$\mathcal{E}_i^{ave} = \frac{1}{10} \sum_{j=1}^{10} \mathcal{E}_i^j. \tag{47}$$

All the values of the dissipation rate are very close to each other, the standard deviation being $\sigma = 5\%$. A larger scattering is observed on the coefficient of determination which, regardless, remains very close to 1. We note also that the mean value of the dissipation rates $\frac{1}{10} \sum_j \bar{\mathcal{P}}^j / \Delta\mathcal{P} = -2.780$ is equal to the dissipation rate of the ensemble average curve reported in Table I, that is $\bar{\mathcal{P}}^{ave} / \Delta\mathcal{P} = -2.780$.

In Fig. 17 the energy dissipation without its linear component $(\mathcal{E} - \bar{\mathcal{P}}t)$, is reported for two realizations, namely N. 2 and N. 9, and for the ensemble average curve. The two realizations have been chosen to represent, respectively, the maximum, N. 9, and the minimum, N. 2, and error

Label $N = 100$	N.1	N.2	N.3	N.4	N.5	N.6	N.7	N.8	N.9	N.10	Series Average
$-\bar{\mathcal{P}}/\Delta\mathcal{P}$	2.90	2.78	2.79	2.82	2.74	2.78	2.74	2.78	2.75	2.73	2.78
$(1 - R^2) \cdot 10^5$	8.8	6.2	12.4	9.5	6.8	11.1	34.5	21.2	37.3	34.5	1.9

TABLE I: Averaged dissipation rates $\bar{\mathcal{P}}$ and coefficients of determination for the series of $N = 100$ simulations.
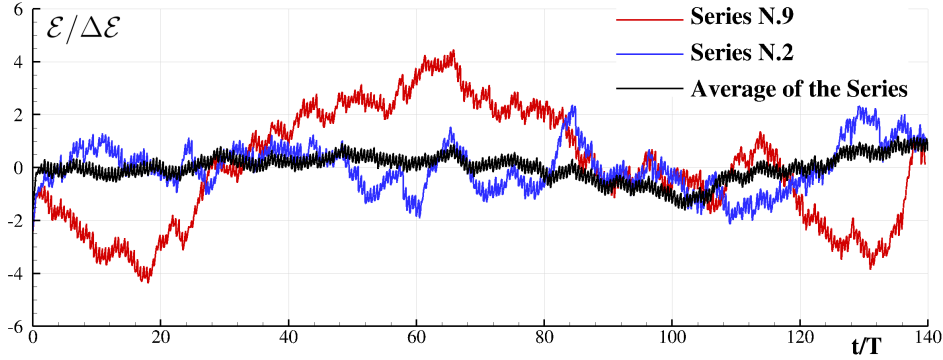
35

FIG. 17: History of the energy dissipation without its linear component $\bar{\mathcal{P}} t$ for simulations N.2 (blue line), N.9 (red line) and the ensemble average of the series (black line). See Table I for label references.

with respect to the linear fit. The average curve is the one exhibiting only small deviations with respect to the horizontal axis, having the highest R^2 value. Conversely, both series N. 2 and N. 9 present remarkable deviations which are distributed on different time scales and amplitudes. This plot highlights the chaotic nature of the solution: the two energy curves diverge just after the first impact and then oscillate around the average dissipation rate. The same holds for all the other realizations of the series. This reflects the fact that, even if the flow characteristics can be locally very different, global quantities, such as the rate of energy dissipation, are affected little.

G. Convergence analysis

In Fig. 18 the convergence study for this test is reported. Particle resolutions corresponding to $N = 25, 50, 100$ are adopted. A number of 10 realizations have been performed and the plotted line represents the ensemble average for each case. In the same Fig. 18 the standard deviation is also reported and represented as an error bar. Remarkably, the standard deviation decreases towards zero as the resolution increases. This result indicates that when increasing the resolution the main eddies driving the energy dissipation are better captured, and thus, the uncertainty of the obtained solution is markedly reduced. Notwithstanding, the computation is still far from numerical convergence. In Sec. VII D it has been highlighted that at least a resolution of $N = 100$ is needed to correctly apply the LES model. This means that for $N = 50$ and $N = 25$ the resolution is too coarse to represent the main vortical structures of the flow.

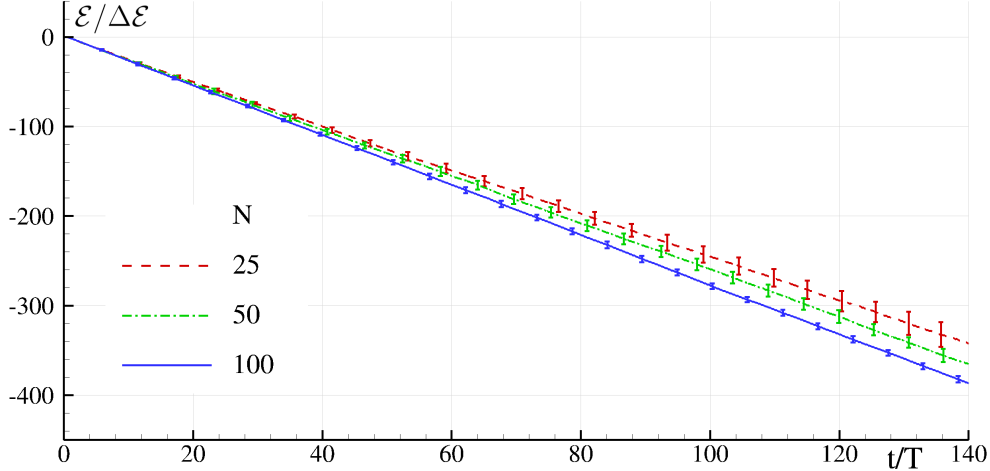To complete the analysis simulations with spatial resolution equal to $N = 200, 400, 800$ have

36

FIG. 18: Ensemble average of the energy dissipation time history for the three resolutions $N = 25, 50, 100$. Error bars refer to the computed standard deviation. For the $N = 200$ simulation only a single realization is reported.

been also performed. However, because of the larger CPU costs only a single simulation has been realized, and smaller number of periods are considered, in particular the time ranges used are $140T, 70T, 20T$ respectively for $N = 200, 400, 800$. Since the standard deviation shown in figure 18 decreases with N and for $N = 100$ is quite small this allow to avoid the evaluation of the ensemble average for the three highest resolutions.

In Fig. 19 the convergence of the average rate of dissipation $\bar{\mathcal{P}}$ is reported for all the six spatial resolutions considered. This has been computed by evaluating the rate of dissipation for each motion period and then averaging over all the simulated periods. In the same plot the error bars refer to the standard deviation. Note that only for the $N = 800$ the predicted $\bar{\mathcal{P}}$ is close to the previous discretization level. This is in agreement with the analysis performed in section VII D where it is shown that for the spatial resolution $N = 800$ the inertial range is well resolved. For a final confirm of this result a simulation with $N = 1600$ is required but this is beyond our available computing resources. Further considerations on the convergence of the numerical results will be addressed in the second part of this paper (Part II) where a decay tank motion is considered for two different Reynolds numbers, i.e. 233,000 and 4,660.

It is worth noting that using the 1D inelastic theory by [15] recalled in section VII C, the predicted dissipation rate is $\mathcal{P}/\Delta\mathcal{P} = -4.6$. This value is about 45% higher (in absolute value) than the one shown in figure 19 for the δ-LES-SPH using the highest spatial resolution $N = 800$.
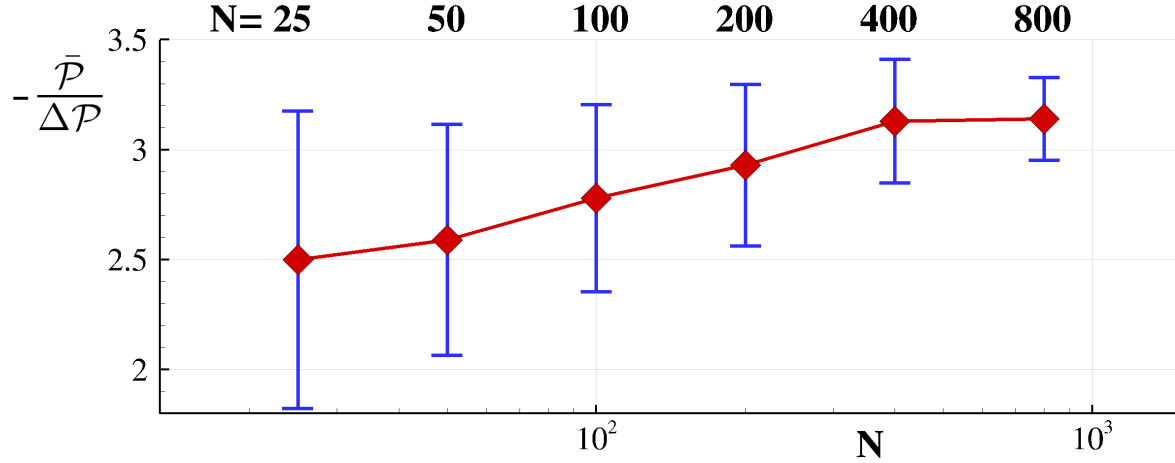
FIG. 19: Average dissipation rates $\bar{\mathcal{P}}$ for resolutions $N = 25, 50, 100, 200, 400, 800$. The Error bars refer to the computed standard deviation for $\bar{\mathcal{P}}$ evaluated at each semi-period of the tank oscillation. For the higher resolution $N = 400$ and 800, because of the too high CPU costs, only 20 oscillations are simulated.

Regarding the CPU costs, to perform the 32 simulations ten cluster nodes equipped with dual 12-core Intel Xeon (Haswell) E5-2680v3 processors 2.5 GHz, was used for 14 days. The only simulation with N=800 (20 oscillation periods) takes 5 days using the ten cluster nodes (*i.e.* 240 cores).

VIII. CONCLUSIONS

A particular case of sloshing has been numerically studied in this work, where the quantification of the mechanisms of the energy dissipation in the fluid is the main objective. The main particularities of this case are: first, its vertical movement with high frequency and acceleration; second, the violent impacts of the highly fragmented free surface against the tank walls; and third, the turbulent dissipation present in this highly detached flow. To study this problem, a 2D single-phase weakly-compressible SPH method with LES modelling, namely δ-LES SPH, has been adopted. The latter is a robust numerical scheme without the presence of tensile instability, for which each term of the total system energy can be directly evaluated. In this framework, the energy dissipation due to numerical, turbulent and viscous effects has been monitored and compared to other more classical SPH schemes and simplified formulations. After monitoring the energy evolution at very different time scales, the fluid impacts are clearly detected as energy

drops at short time scales and turbulent dissipation is identified as the leading energy sink. On the other hand, in the long time scale, a constant rate of the energy dissipation is clearly observed which is not dependent on the local flow features. This observation is further supported by repeating the simulations and applying small differences, on the initial particle setup, where local solutions show local important differences but without a strong impact on global quantities such as the energy dissipation rate. A discussion about how the resolution affects this apparent presence of chaos in the problem is proposed. Whilst assuming that the resolution is not enough for numerical convergence, the uncertainty is clearly reduced when the number of particles is increased. The present work is completed with the other damped and FSI cases as well as experimental comparisons, all of them conducted in the second part (Part II) of this paper series.

IX. ACKNOWLEDGEMENTS

[1] S. Silverman, H.N. Abramson, The dynamic behaviour of liquids in moving containers. NASA SP-106, 1966.

[2] M. Antuono, A. Colagrossi, and S. Marrone. Numerical diffusive terms in weakly-compressible SPH schemes. *Computer Physics Communications*, 183(12):2570–2580, 2012.

[3] M. Antuono, A. Colagrossi, S. Marrone, and D. Molteni. Free-surface flows solved by means of SPH schemes with numerical diffusive terms. *Computer Physics Communications*, 181(3):532–549, 2010.

[4] M. Antuono, S. Marrone, A. Colagrossi, and B. Bouscasse. Energy balance in the δ-SPH scheme. *Computer Methods in Applied Mechanics and Engineering*, 289:209–226, 2015.

[5] M. Antuono, S. Marrone, A. Di Mascio, and A. Colagrossi. Smoothed particle hydrodynamics method from a large eddy simulation perspective. generalization to a quasi-lagrangian model. *Physics of Fluids*, 33(1):015102, 2021.

[6] M. Antuono, P.N. Sun, S. Marrone, and A. Colagrossi. The δ-ALE-SPH model: An arbitrary lagrangian-eulerian framework for the δ-SPH model with particle shifting technique. *Computers & Fluids*, 216:104806, 2021.

[7] B. Bouscasse, A. Colagrossi, A. Souto-Iglesias, and J.L. Cercos-Pita. Mechanical energy dissipation induced by sloshing and wave breaking in a fully coupled angular motion system. i. theoretical formulation and numerical investigation. *Physics of Fluids*, 26(3):033103, 2014.

[8] B. Bouscasse, A. Colagrossi, A. Souto-Iglesias, and J.L. Cercos-Pita. Mechanical energy dissipation induced by sloshing and wave breaking in a fully coupled angular motion system. ii. experimental investigation. *Physics of Fluids*, 26(3):033104, 2014.

[9] J. Calderon-Sanchez, J. Martinez-Carrascal, L.M. Gonzalez-Gutierrez, and A. Colagrossi. A global analysis of a coupled violent vertical sloshing problem using an sph methodology. *Engineering Applications of Computational Fluid Mechanics*, 15(1):865–888, 2021.

[10] P.A. Caron, M.A. Cruchaga, and A.E. Larreteguy. Study of 3d sloshing in a vertical cylindrical tank. *Physics of Fluids*, 30(8):082112, 2018.

[11] J.L. Cercos-Pita, M. Antuono, A. Colagrossi, and A. Souto-Iglesias. SPH energy conservation for fluid–solid interactions. *Computer Methods in Applied Mechanics and Engineering*, 317:771–791, 2017.

[12] E.D. Christensen. Large eddy simulation of spilling and plunging breakers. *Coastal Engineering*, 53(5-6):463–485, 2006.

[13] E.D. Christensen and R. Deigaard. Large eddy simulation of breaking waves. *Coastal engineering*, 42(1):53–86, 2001.

[14] A. Colagrossi, M. Antuono, and D. Le Touzé. Theoretical considerations on the free-surface role in the Smoothed-particle-hydrodynamics model. *Physical Review E*, 79(5):056701, 2009.

[15] L. Constantin, J.J. De Courcy, B. Titurus, T.C.S. Rendall, and J.E. Cooper. Sloshing induced damping across froude numbers in a harmonically vertically excited system. *Journal of Sound and Vibration*, 510:116302, 2021.

[16] M.J. Cooker. Wave energy losses from a suspended container. *Physics of Fluids*, 8:283, 1996.

[17] L. Davidson. Large eddy simulations: how to evaluate resolution. *International Journal of Heat and Fluid Flow*, 30(5):1016–1025, 2009.

[18] J.J. De Courcy, L. Constantin, B. Titurus, T.C.S. Rendall, and J.E. Cooper. Sloshing induced damping in vertically vibrating systems. In *IOP Conference Series: Materials Science and Engineering*, volume 1024, page 012084. IOP Publishing, 2021.

[19] L. Delorme, A. Colagrossi, A. Souto-Iglesias, R. Zamora-Rodriguez, and E. Botia-Vera. A set of canonical problems in sloshing, part i: Pressure field in forced rollâ€"comparison between experimental results and sph. *Ocean Engineering*, 36(2):168–178, 2009.

[20] Z. Demirbilek. Energy dissipation in sloshing waves in a rolling rectangular tankâ€"i. mathematical theory. *Ocean Engineering*, 10(5):347–358, 1983.

[21] A. Di Mascio, M. Antuono, A. Colagrossi, and S. Marrone. Smoothed particle hydrodynamics method from a large eddy simulation perspective. *Physics of Fluids*, 29(3):035102, 2017.

[22] A. Di Mascio, M. Antuono, A. Colagrossi, and S. Marrone. Smoothed particle hydrodynamics method from a large eddy simulation perspective. *Physics of Fluids*, 29(3):035102, 2017.

[23] O.M. Faltinsen and A.N. Timokha. *Sloshing*. Cambridge University Press, 2009.

[24] F. Gambioli, A. Chamos, S. Jones, P. Guthrie, J. Webb, J. Levenhagen, P. Behruzi, F. Mastroddi, A. Malan, S. Longshaw, et al. Sloshing wing dynamics–project overview. *Proceedings of 8th Transport Research Arena TRA 2020, April 27-30, 2020, Helsinki, Finland*, 2020.

[25] F. Gambioli and A. Malan. Fuel loads in large civil airplanes. In *International Forum on Aeroelasticity and Structural Dynamics IFASD 2017*, 2017.

[26] J.M. Gimenez and L.M. González. An extended validation of the last generation of particle finite element method for free surface flows. *Journal of Computational Physics*, 284:186–205, 2015.

[27] R.A. Gingold and J.J. Monaghan. Smoothed Particle Hydrodynamics: theory and application to non-spherical stars. *Mon. Not. Roy. Astron. Soc. (MNRAS)*, 181:375–389, 1977.

[28] H. Gotoh, A. Khayyer, H. Ikari, T. Arikawa, and K. Shimosako. On enhancement of incompressible sph method for simulation of violent sloshing flows. *Applied Ocean Research*, 46:104–115, 2014.

[29] M.D. Green and J. Peiró. Long duration sph simulations of sloshing in tanks with a low fill ratio and high stretching. *Computers & Fluids*, 174:179–199, 2018.

[30] K. Hanjalić and B. Launder. *Modelling turbulence in engineering and the environment: second-moment routes to closure*. Cambridge university press, 2011.

[31] E. Labourasse, D. Lacanette, A. Toutant, P. Lubin, S. Vincent, O. Lebaigue, J.P. Caltagirone, and P. Sagaut. Towards large eddy simulation of isothermal two-phase flows: Governing equations and a priori tests. *International journal of multiphase flow*, 33(1):1–39, 2007.

[32] P. Lubin and S. Glockner. Numerical simulations of three-dimensional plunging breaking waves: generation and evolution of aerated vortex filaments. *Journal of Fluid Mechanics*, 767:364–393, 2015.

[33] P. Lubin, S. Vincent, S. Abadie, and J.P. Caltagirone. Three-dimensional large eddy simulation of air entrainment under plunging breaking waves. *Coastal engineering*, 53(8):631–655, 2006.

[34] L.B. Lucy. A numerical approach to the testing of the fission hypothesis. *Astronomical Journal*, 82:1013–1024, 1977.

[35] S. Marrone, A. Colagrossi, A. Di Mascio, and D. Le Touzé. Prediction of energy losses in water impacts using incompressible and weakly compressible models. *Journal of Fluids and Structures*, 54:802–822, 2015.

[36] S. Marrone, A. Colagrossi, A. Di Mascio, and D. Le Touzé. Analysis of free-surface flows through energy considerations: Single-phase versus two-phase modeling. *Phys. Rev. E*, 93:053113, May 2016.

[37] J. Martinez-Carrascal and L.M. Gonzalez-Gutierrez. Experimental study of the liquid damping effects on a sdof vertical sloshing tank. *Journal of fluids and structures*, 100, 2021.

[38] D.D. Meringolo, A. Colagrossi, S. Marrone, and F. Aristodemo. On the filtering of acoustic components in weakly-compressible SPH simulations. *Journal of Fluids and Structures*, 70:1–23, 2017.

[39] D.D. Meringolo, S. Marrone, A. Colagrossi, and Y. Liu. A dynamic δ-sph model: How to get rid of diffusive parameter tuning. *Computers & Fluids*, 179:334–355, 2019.

[40] J.J. Monaghan. Simulating Free Surface Flows with SPH. *J. Comp. Phys.*, 110(2):39–406, 1994.

[41] J.J. Monaghan. SPH without a tensile instability. *J. Comp. Phys.*, 159(2):290–311, 2000.

[42] S. Nath, N. Debnath, and S. Choudhury. Methods for improving the seismic performance of structures-a review. In *IOP Conference Series: Materials Science and Engineering*, volume 377, page 012141. IOP Publishing, 2018.

[43] M. Pizzoli, F. Saltari, F. Mastroddi, J.M. Carrascal, and L.M. González-Gutiérrez. Nonlinear reduced-order model for vertical sloshing by employing neural networks. *Nonlinear Dynamics*, pages 1–10, 2021.

[44] S.B. Pope. Ten questions concerning the large-eddy simulation of turbulent flows. *New journal of Physics*, 6(1):35, 2004.

[45] D. Reed, J. Yu, H. Yeh, and S. Gardarsson. Investigation of tuned liquid dampers under large amplitude excitation. *Journal of Engineering Mechanics*, 124(4):405–413, 1998.

[46] J.R. Shao, H.Q. Li, G.R. Liu, and M.B. Liu. An improved sph method for modeling liquid sloshing dynamics. *Computers & Structures*, 100:18–26, 2012.

[47] J. Smagorinsky. General circulation experiments with the primitive equations: I. the basic experiment. *Monthly weather review*, 91(3):99–164, 1963.

[48] J. Stasch, B. Avci, and P. Wriggers. Numerical simulation of fluid-structure interaction problems by a coupled sph-fem approach. *Proc. Appl. Math. Mech.*, 16(1):491–492, 2016.

[49] L.M. Sun and Y. Fujino. A semi-analytical model for tuned liquid damper (tld) with wave breaking. *Journal of Fluids and Structures*, 8(5):471–488, 1994.

[50] P.N. Sun, A. Colagrossi, S. Marrone, M. Antuono, and A.M. Zhang. A consistent approach to particle shifting in the δ-plus-SPH model. *Computer Methods in Applied Mechanics and Engineering*, 348:912–934, 2019.

[51] P.N. Sun, A. Colagrossi, S. Marrone, M. Antuono, and A.M. Zhang. Multi-resolution delta-plus-SPH with tensile instability control: Towards high reynolds number flows. *Computer Physics Communications*, 224:63–80, 2018.

[52] W.G. Szymczak. Energy losses in non-classical free surface flows. In J.R. Blake, J.M. Boulton-Stone, and N.H. Thomas, editors, *Bubble Dynamics and Interface Phenomena*, volume 23 of *Fluid Mechanics and Its Applications*, pages 413–420. Springer Netherlands, 1994.

[53] B. Titurus, J.E. Cooper, F. Saltari, F. Mastroddi, and F. Gambioli. Analysis of a sloshing beam experiment. In *International Forum on Aeroelasticity and Structural Dynamics. Savannah, Georgia, USA, paper*, volume 139, 2019.